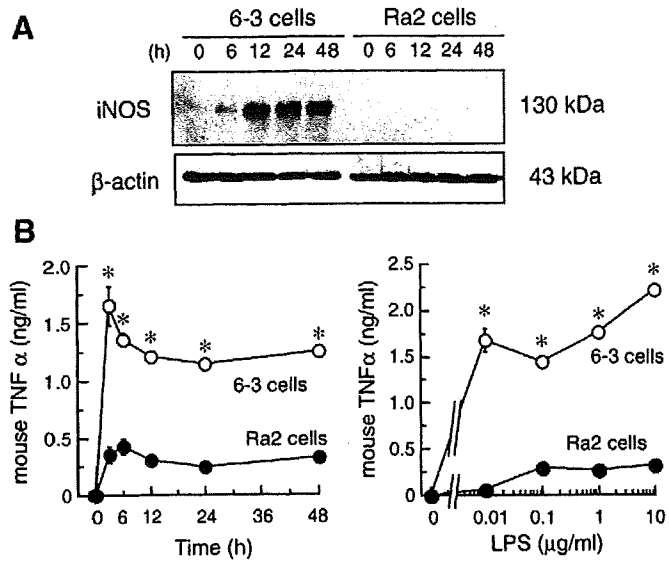

Fig. 7. The induction of iNOS and production of TNFα in LPS-treated mouse MG cell lines 6-3 and Ra2. (A) The cells were treated with LPS (10 μg/ml) for the indicated times, and cell extracts (30 μg of protein) were subjected to an immunoblot analysis using the anti-mouse iNOS monoclonal antibody, or anti-β-actin monoclonal antibody. (B) The cells were treated with LPS (10 μg/ml) for 24 h (Left panel). The cells were treated with various concentrations of LPS for 24 h (Right panel). TNFα in the medium was measured with an ELISA kit. Values were means±SD ($n=3$). *, $p<0.05$, significantly different from Ra2 cells.

CNS and they may have different functions (Bulloch et al., 2008; Elkabes et al., 1996; Ren et al., 1999; Sriram et al., 2006). In the present study, we demonstrated that the established mouse CD40$^+$ MG cell line 6-3 (Kanzawa et al., 2000) also induced iNOS and TNFα more strongly than the mouse CD40$^-$ MG cell line Ra2 after LPS stimulation (Fig. 7). In contrast, we previously showed that CD40$^+$ MG barely responded to an anti-inflammatory cytokine IL-4, whereas CD40$^-$ MG are highly responsive (Shimizu et al., 2008). CD40$^+$ MG are distinct from CD40$^-$ MG in terms of cell surface molecules of CD40 and CD86: CD40$^+$ MG express both molecules, while CD40$^-$ MG express no CD40 and less CD86. Most recently, we have successfully developed a monoclonal antibody that selectively recognizes CD40$^+$ MG and the antigen molecule is distinct from CD40 and CD86 (K. Kawahara et al., manuscript in preparation). Taken together, we consider that there exist at least two subtypes of MG as we separated and they exhibit different inflammatory responses. The conclusion whether two separate MG cell types actually exist in matured brains or they are certainly explained in terms of different cellular maturities can wait until the cell lineage of these MG is clarified, but the subject is obviously important since manipulation of the MG with either separate types or different states may bear on therapeutic strategies for many neurological diseases.

In summary, we demonstrated that one possible subtype (CD40$^+$) of MG, by comparison to another subtype (CD40$^-$), produced a larger amount of NO and TNFα, both of which were mediated by easier breakdown of the phosphorylated IκBα. The CD40$^+$ MG may exhibit neurotoxic action under certain pathological conditions in brains.

Acknowledgements

We thank Dr. T. Shuto (Kumamoto University) for suggestions and discussion. This work was supported, in part, by Grants-in-Aid for scientific research (to K. K. and H. N.) and for Scientific Research of Priority Area "Neuron-Glia Network" (to H. N.) from the Ministry of Education, Culture, Sports, Science and Technology of Japan.

References

Andjelkovic, A.V., Nikolic, B., Pachter, J.S., Zecevic, N., 1998. Macrophages/microglial cells in human central nervous system during development: an immunohistochemical study. Brain Res. 814, 13–25.
Bagasra, O., Michaels, F.H., Zheng, Y.M., Bobroski, L.E., Spitsin, S.V., Fu, Z.F., Tawadros, R., Koprowski, H., 1995. Activation of the inducible form of nitric oxide synthase in the brains of patients with multiple sclerosis. Proc. Natl. Acad. Sci. U. S. A. 92, 12041–12045.
Banati, R.B., Gehrmann, J., Schubert, P., Kreutzberg, G.W., 1993. Cytotoxicity of microglia. Glia 7, 111–118.
Barone, F.C., Arvin, B., White, R.F., Miller, A., Webb, C.L., Willette, R.N., Lysko, P.G., Feuerstein, G.Z., 1997. Tumor necrosis factor-alpha. A mediator of focal ischemic brain injury. Stroke 28, 1233–1244.
Bulloch, K., Miller, M.M., Gal-Toth, J., Milner, T.A., Gottfried-Blackmore, A., Waters, E.M., Kaunzner, U.W., Liu, K., Lindquist, R., Nussenzweig, M.C., Steinman, R.M., McEwen, B.S., 2008. CD11c/EYFP transgene illuminates a discrete network of dendritic cells within the embryonic, neonatal, adult, and injured mouse brain. J. Comp. Neurol. 508, 687–710.
Chan, W.Y., Kohsaka, S., Rezaie, P., 2007. The origin and cell lineage of microglia: new concepts. Brain Res. Rev. 53, 344–354.
Colton, C., Wilt, S., Gilbert, D., Chernyshev, O., Snell, J., Dubois-Dalcq, M., 1996. Species differences in the generation of reactive oxygen species by microglia. Mol. Chem. Neuropathol. 28, 15–20.
Dickson, D.W., Lee, S.C., Mattiace, L.A., Yen, S.H., Brosnan, C., 1993. Microglia and cytokines in neurological disease, with special reference to AIDS and Alzheimer's disease. Glia 7, 75–83.
Ding, M., St. Pierre, B.A., Parkinson, J.F., Medberry, P., Wong, J.L., Rogers, N.E., Ignarro, L.J., Merrill, J.E., 1997. Inducible nitric-oxide synthase and nitric oxide production in human fetal astrocytes and microglia. A kinetic analysis. J. Biol. Chem. 272, 11327–11335.
Elkabes, S., DiCicco-Bloom, E.M., Black, I.B., 1996. Brain microglia/macrophages express neurotrophins that selectively regulate microglial proliferation and function. J. Neurosci. 16, 2508–2521.
González-Scarano, F., Baltuch, G., 1999. Microglia as mediators of inflammatory and degenerative diseases. Annu. Rev. Neurosci. 22, 219–240.
Hanisch, U.K., Kettenmann, H., 2007. Microglia: active sensor and versatile effector cells in the normal and pathologic brain. Nat. Neurosci. 10, 1387–1394.
Hatada, E.N., Krappmann, D., Scheidereit, C., 2000. NF-kappaB and the innate immune response. Curr. Opin. Immunol. 12, 52–58.
Hayes, G.M., Woodroofe, M.N., Cuzner, M.L., 1987. Microglia are the major cell type expressing MHC class II in human white matter. J. Neurol. Sci. 80, 25–37.
Haynes, R.L., Folkerth, R.D., Keefe, R.J., Sung, I., Swzada, L.I., Rosenberg, P.A., Volpe, J.J., Kinney, H.C., 2003. Nitrosative and oxidative injury to premyelinating oligodendrocytes in periventricular leukomalacia. J. Neuropathol. Exp. Neurol. 62, 441–450.
Hibbs Jr., J.B., Taintor, R.R., Vavrin, Z., 1987. Macrophage cytotoxicity: role for L-arginine deiminase and imino nitrogen oxidation to nitrite. Science 235, 473–476.
Ignarro, L.J., 2000. Nitric Oxide: Biology and Pathology. Academic Press, San Diego, CA.
Itagaki, S., McGeer, P.L., Akiyama, H., Zhu, S., Selkoe, D., 1989. Relationship of microglia and astrocytes to amyloid deposits of Alzheimer disease. J. Neuroimmunol. 24, 173–182.
Kanzawa, T., Sawada, M., Kato, K., Yamamoto, K., Mori, H., Tanaka, R., 2000. Differentiated regulation of allo-antigen presentation by different types of murine microglial cell lines. J. Neurosci. Res. 62, 383–388.
Katoh, Y., Niimi, M., Yamamoto, Y., Kawamura, T., Morimoto-Ishizuka, T., Sawada, M., Takemori, H., Yamatodani, A., 2001. Histamine production by cultured microglial cells of the mouse. Neurosci. Lett. 305, 181–184.
Kawahara, K., Mori, M., Nakayama, H., 2004. NO-induced apoptosis and ER stress in microglia. Folia Pharmacol. Jpn. 124, 399–406.
Kreutzberg, G.W., 1996. Microglia: a sensor for pathological events in the CNS. Trends Neurosci. 19, 312–318.
Kuwabara, Y., Yokoyama, A., Yang, L., Toku, K., Mori, K., Takeda, I., Shigekawa, T., Zhang, B., Maeda, N., Sakanaka, M., Tanaka, J., 2003. Two populations of microglial cells isolated from rat primary mixed glial cultures. J. Neurosci. Res. 73, 22–30.
McGeer, P.L., McGeer, E.G., 1995. The inflammatory response system of brain: implications for therapy of Alzheimer and other neurodegenerative diseases. Brain Res. Brain Res. Rev. 21, 195–218.
Merrill, J.E., Ignarro, L.J., Sherman, M.P., Melinek, J., Lane, T.E., 1993. Microglial cell cytotoxicity of oligodendrocytes is mediated through nitric oxide. J. Immunol. 151, 2132–2141.
Muller, J.M., Ziegler-Heitbrock, H.W., Baeuerle, P.A., 1993. Nuclear factor kappa B, a mediator of lipopolysaccharide effects. Immunobiology 187, 233–256.
Nagasaki, A., Gotoh, T., Takeya, M., Yu, Y., Takiguchi, M., Matsuzaki, H., Takatsuki, K., Mori, M., 1996. Coinduction of nitric oxide synthase, argininosuccinate synthetase, and argininosuccinate lyase in lipopolysaccharide-treated rats. RNA blot, immunoblot, and immunohistochemical analyses. J. Biol. Chem. 271, 2658–2662.
Nakajima, K., Kohsaka, S., 2001. Microglia: activation and their significance in the central nervous system. J. Biochem. (Tokyo). 130, 169–175.
Neish, A.S., Gewirtz, A.T., Zeng, H., Young, A.N., Hobert, M.E., Karmali, V., Rao, A.S., Madara, J.L., 2000. Prokaryotic regulation of epithelial responses by inhibition of IkappaB-alpha ubiquitination. Science 289, 1560–1563.
Okada, M., Irie, S., Sawada, M., Urae, R., Urae, A., Iwata, N., Ozaki, N., Akazawa, K., Nakanishi, H., 2003. Pepstatin A induces extracellular acidification distinct from aspartic protease inhibition in microglial cell lines. Glia 43, 167–174.
Ren, L., Lubrich, B., Biber, K., Gebicke-Haerter, P.J., 1999. Differential expression of inflammatory mediators in rat microglia cultured from different brain regions. Brain Res. Mol. Brain Res. 65, 198–205.

Saura, J., Tusell, J.M., Serratosa, J., 2003. High-yield isolation of murine microglia by mild trypsinization. Glia 44, 183–189.
Sawada, M., Suzumura, A., Yamamoto, H., Marunouchi, T., 1990. Activation and proliferation of the isolated microglia by colony stimulating factor-1 and possible involvement of protein kinase C. Brain Res. 509, 119–124.
Sawada, M., Suzumura, A., Marunouchi, T., 1995. Cytokine network in the central nervous system and its roles in growth and differentiation of glial and neuronal cells. Int. J. Dev. Neurosci. 13, 253–264.
Sawada, M., Imamura, K., Nagatsu, T., 2006. Role of cytokines in inflammatory process in Parkinson's disease. J. Neural Transm., Suppl. 70, 373–381.
Schwartz, M., Butovsky, O., Bruck, W., Hanisch, U.K., 2006. Microglial phenotype: is the commitment reversible? Trends Neurosci. 29, 68–74.
Shimizu, E., Kawahara, K., Kajizono, M., Sawada, M., Nakayama, H., 2008. Il-4-induced selective clearance of oligomeric β-amyloid peptide$_{1-42}$ by rat type-2 microglia. J. Immunol. 181, 6503–6513.
Sriram, K., Matheson, J.M., Benkovic, S.A., Miller, D.B., Luster, M.I., O'Callaghan, J.P., 2006. Deficiency of TNF receptors suppresses microglial activation and alters the susceptibility of brain regions to MPTP-induced neurotoxicity: role of TNF-α. FASEB J. 20, 670–682.
Suzuki, T., Hide, I., Ido, K., Kohsaka, S., Inoue, K., Nakata, Y., 2004. Production and release of neuroprotective tumor necrosis factor by P2X7 receptor-activated microglia. J. Neurosci. 24, 1–7.
Suzumura, A., Mezitis, S.G., Gonatas, N.K., Silberberg, D.H., 1987. MHC antigen expression on bulk isolated macrophage-microglia from newborn mouse brain: induction of Ia antigen expression by gamma-interferon. J. Neuroimmunol. 15, 263–278.
Suzumura, A., Sawada, M., Takayanagi, T., 1998. Production of interleukin-12 and expression of its receptors by murine microglia. Brain Res. 787, 139–142.
Vodovotz, Y., Lucia, M.S., Flanders, K.C., Chesler, L., Xie, Q.W., Smith, T.W., Weidner, J., Mumford, R., Webber, R., Nathan, C., Roberts, A.B., Lippa, C.F., Sporn, M.B., 1996. Inducible nitric oxide synthase in tangle-bearing neurons of patients with Alzheimer's disease. J. Exp. Med. 184, 1425–1433.
Walker, D.G., Kim, S.U., McGeer, P.L., 1995a. Complement and cytokine gene expression in cultured microglial derived from postmortem human brains. J. Neurosci. Res. 40, 478–493.
Walker, W.S., Gatewood, J., Olivas, E., Askew, D., Havenith, C.E., 1995b. Mouse microglial cell lines differing in constitutive and interferon-gamma-inducible antigen-presenting activities for naive and memory CD4+ and CD8+ T cells. J. Neuroimmunol. 63, 163–174.

Published August 31, 2009

ARTICLE

Temperature dependence of proton permeation through a voltage-gated proton channel

Miyuki Kuno,[1,2] Hiroyuki Ando,[3] Hirokazu Morihata,[1] Hiromu Sakai,[1] Hiroyuki Mori,[1] Makoto Sawada,[4] and Shigetoshi Oiki[3]

[1]Department of Physiology, Osaka City University Graduate School of Medicine, Abeno-ku, Osaka 545-8585, Japan
[2]Division of Intracellular Metabolism, National Institute for Physiological Sciences, Okazaki 444-8585, Japan
[3]Department of Molecular Physiology and Biophysics, Faculty of Medical Sciences, University of Fukui, Fukui 910-1193, Japan
[4]Department of Brain Life Science, Research Institute of Environmental Medicine, Nagoya University, Nagoya 464-8601, Japan

Voltage-gated proton channels are found in many different types of cells, where they facilitate proton movement through the membrane. The mechanism of proton permeation through the channel is an issue of long-term interest, but it remains an open question. To address this issue, we examined the temperature dependence of proton permeation. Under whole cell recordings, rapid temperature changes within a few milliseconds were imposed. This method allowed for the measurement of current amplitudes immediately before and after a temperature jump, from which the ratios of these currents (I_{ratio}) were determined. The use of I_{ratio} for evaluating the temperature dependence minimized the contributions of factors other than permeation. Temperature jumps of various degrees (ΔT, −15 to 15°C) were applied over a wide temperature range (4–49°C), and the Q_{10}s for the proton currents were evaluated from the I_{ratio}s. Q_{10} exhibited a high temperature dependence, varying from 2.2 at 10°C to 1.3 at 40°C. This implies that processes with different temperature dependencies underlie the observed Q_{10}. A novel resistivity pulse method revealed that the access resistance with its low temperature dependence predominated in high temperature ranges. The measured temperature dependence of Q_{10} was decomposed into Q_{10} of the channel and of the access resistances. Finally, the Q_{10} for proton permeation through the voltage-gated proton channel itself was calculated and found to vary from 2.8 at 5°C to 2.2 at 45°C, as expected for an activation enthalpy of 64 kJ/mol. The thermodynamic features for proton permeation through proton-selective channels were discussed for the underlying mechanism.

INTRODUCTION

Proton transfer across biological membranes is performed by various types of membrane proteins, including pumps, transporters, and channels. Of these, channels are the most efficient pathway for ion transfer. The voltage-gated proton channel described initially in snail neurons (Thomas and Meech, 1982) had activation gating at depolarized potentials similar to most of the voltage-gated cation channels. The proton channel is almost perfectly selective for protons. These channels have been found in many types of cells, including phagocytes (e.g., microglia), osteoclasts, and epithelial cells. Fast proton transfer is thought to be a prerequisite to cellular processes, such as phagocytosis (Henderson et al., 1987).

The whole cell currents of the voltage-gated proton channel exhibit an unusually high temperature dependence (Byerly and Suen, 1989; Kuno et al., 1997; DeCoursey and Cherny, 1998). The high Q_{10}s (three to five) of the measured currents have been related to temperature dependence of proton permeation (DeCoursey and Cherny, 1998), which further suggests that protons may permeate through the channel with "unusually" high temperature-dependent processes compared with those of other types of channels (DeCoursey, 2003). This conjecture, however, still remains an open question because features of the proton channel have made quantitative evaluations of the temperature dependence difficult. Among other things, the single-channel conductance of the proton channel is of the order of femto Siemens (Cherny et al., 2003), so that an evaluation of changes in conductance necessitates whole cell recordings. We have observed, however, that the proton currents vary in amplitudes, even at a fixed temperature (Morihata et al., 2000a). This phenomenon can be explained by an alteration in the number of activatable channels upon repeated application of depolarization pulses being compatible with the results observed for other types of membrane proteins (Morgan et al., 2003). These features of the channel raise concerns as to whether the reported temperature dependence actually reflects that of permeation through the channel.

Correspondence to Shigetoshi Oiki: oiki-fki@umin.ac.jp
Abbreviation used in this paper: gA, gramicidin A.

The Rockefeller University Press $30.00
J. Gen. Physiol. Vol. 134 No. 3 191–205
www.jgp.org/cgi/doi/10.1085/jgp.200910213

Published August 31, 2009

To address the permeation issues of proton channels, the consideration of the physicochemical principles for proton transfer is crucial. In bulk solution, proton transfer is characterized by the Grotthuss mechanism (de Grotthuss, 1806; Eigen, 1964; Agmon, 1995, 1996, 1999; Robinson and Stokes, 2002; Swanson et al., 2007) and buffered diffusion (Eigen et al., 1964; Keener and Sneyd, 1998; Swietach et al., 2003; Zifarelli et al., 2008). These additional "proton-specific" factors modify channel access resistance, the concentration polarization at the cell membrane, and changes in ion concentration in the cytosol, factors expected to affect the properties of ion permeation through all types of channels. Each issue has been studied separately (DeCoursey and Cherny, 1996; Gordienko et al., 1996), but the findings have not been integrated to produce a picture of the whole process of proton permeation. For example, the magnitudes of the measured currents may be determined, in part, by proton-transfer processes outside the channel molecule, and the proton fluxes may cause local concentration changes (decreases at the "upstream" membrane–solution interface and increases at the "downstream" membrane–solution interface). These interrelated issues should be treated in a systematic manner with quantitative evaluation. To this end, the theoretical basis for the proton-transfer processes was reviewed to estimate the relative contributions of proton-transfer events, which were exploited for the experimental design.

Experimental strategy

Protons are transferred from the bulk solution to the channel entrance through the access region, which induces depletion of protons upstream and accumulation downstream in the bulk, in the vicinity of the membrane, and at the channel entrance. These events, which develop with spatially different scales, are termed as the bulk concentration change, concentration polarization, and access resistance. For the proton channels, experiments were performed in the presence of low concentrations of protons and high concentrations of buffer. The latter was a prerequisite as a resource of the proton reservoir, which helps the proton flux to endure under the limited supply from the patch pipette. Even if the high concentration buffer facilitates proton transfer in bulk solutions (Keener and Sneyd, 1998), the persistent efflux eventually leads to cytosolic depletion of the proton concentration (concentration polarization and depletion of the cytosolic concentration) (Gordienko et al., 1996). Recently, local changes in proton concentration were estimated by Zifarelli et al. (2008) using a simulation technique at low buffer concentrations. Following their method, we estimated the time courses of the concentrations in our highly buffered experimental conditions (see Appendix). The changes of pH at the vicinity of the membrane during maximum currents in our experiments were negligible, and their time courses were several tens of milliseconds. These predictions, especially for the time order of development, were important considerations for experimental design.

To address the proton-transfer process at the molecular level, the concentration profiles of protons treated with a one-dimensional regimen are no longer valid (Berg and Purcell, 1977). At the pore entrance, proton fluxes converge and proton depletion develops locally when the transfer of ions within the pore occurs at a faster rate than diffusion toward the pore. This diffusion-limited process in the vicinity of the pore and the convergence of ion trajectories toward the narrow pore opening lead to additional resistance outside the channel pore (access resistance [R_{AR}]) (Hille, 1968; Hall, 1975; Läuger, 1976; Andersen, 1983; Hladky, 1984; Peskoff and Bers, 1988; Aguilella-Arzo et al., 2005). The theory estimated that the development of the access resistance is very fast (10^{-10} s; see Appendix) (Crank, 1975) compared with the accessible speed of electrophysiological measurements (see Appendix).

Each of these proton-specific issues developing outside of the channel should contribute somewhat to the measured proton currents. We focused on the large discrepancies in time scale for the development of each event. The concentration polarization and bulk depletion develop on the order of a second or slower. Therefore, if we change the temperature of the channel in a rapid stepwise manner and measure the changes in proton current immediately before and after the step, the measured current changes are little affected by slowly developing events. In the present study, stepwise changes in temperature for a cell undergoing whole cell current recording were applied within a few milliseconds by the pulse method (Ando et al., 2005). This rapid system enabled experiments in a wide temperature range and repeated applications of temperature changes for a single cell under patch clamp. Furthermore, the temperature changes were rapid enough to minimize changes in the gating status because the voltage-gated proton channel exhibits slow activation gating (several tens or hundreds of milliseconds).

The next issue to be addressed was to determine the contribution of the access resistance to the total resistance. The access resistance grows with a time constant of 10^{-10} s and cannot be discriminated by the "rapid" temperature change method. Here, we exploited the facts that (1) R_{AR} changes with the resistivity of the bulk solution (Hall, 1975), (2) R_{AR} for the extracellular side can be changed by perfusing extracellular solution, and (3) changes in R_{AR} leads to changes in R_{total}. Therefore, measuring changes in R_{total} upon perturbation of the extracellular solution would provide estimates of the relative contribution of R_{AR} to R_{total}. We applied a resistivity pulse method and estimated the ratio of R_{AR} to R_{Ch}, the value of which was used to decompose the temperature dependence of the proton channel.

Published August 31, 2009

With all appropriate caveats in mind, the native proton channel expressed in microglial cells was examined. We have elucidated the temperature dependence of proton permeation through the voltage-gated proton channel.

MATERIALS AND METHODS

Electrophysiology

Rat microglia (GMI-R1) (Sawada et al., 1998) were cultured in Dulbecco's modified Eagle's medium supplemented with granulocyte/macrophage colony-stimulating factor, glucose, and insulin. Whole cell recordings were performed with an AxoPatch 200B amplifier (MDS Analytical Technologies). Currents were filtered at 1 kHz and sampled at 5 kHz with DigiData1322A (MDS Analytical Technologies). The pipette solution contained 120 mM Mes, 65 mM NMDG aspartate, 3 mM $MgCl_2$, 1 mM BAPTA, and 1 mM Na_2ATP, pH 5.5–6.2. The extracellular solution contained 100 mM HEPES, 75 mM NMDG aspartate, 1 mM $CaCl_2$, 1 mM $MgCl_2$, and 50 μM 4,4'-diisothiocyanatostilbene-2,2'-disulphonic acid (DIDS). The pH (7.3) was adjusted by CsOH. Pipette resistances ranged between 5 and 15 MΩ.

Estimation of the shift of the reversal potential

The reversal potentials (V_{rev}s) were estimated from two methods, one from the I-V curve and another from current measurements at two different membrane potentials. The I-V curves were obtained as follows. Ramp potentials were applied at the end of a long depolarization pulse and at the end of a mock 10-ms depolarization pulse. Ramp current traces after the long depolarization pulse were subtracted by those for a mock 10-ms depolarization pulse. In the second method, V_{rev} was estimated from the current amplitudes at two different membrane potentials. Proton currents were elicited by a depolarization pulse to 0 mV (V_{Depo}), and then repolarized to −40 mV (V_{Tail}). The reversal potentials were interpolated from the current amplitudes at the end of the depolarization pulse (I_{Depo}) and at the peak of the tail current (I_{Tail}) using the following equation.

$$V_{rev} = -\frac{V_{Depo} - V_{Tail}}{1 - I_{Tail} / I_{Depo}} \quad (1)$$

Temperature pulse experiments

A rapid temperature pulse system was built with the ultrafast solution-switching system (LSS-3200; EXFO) equipped with a double-barreled tube from which solutions of different temperatures were perfused (Fig. 1 A). The system (Ando et al., 2005) included (1) a piezoelectric device (LSS-3200; EXFO) to shift the outflow, (2) a double-barreled tube (the temperatures of the outflows were controlled independently), (3) a patch-clamped microglia, and (4) an ultrafine thermocouple (ANBE SMT Ltd.). Two solutions of different temperatures flowed at rates of 3–6 μl/s (an injection pump; TE-221; Terumo). A voltage-clamped microglial cell was placed in the midst of one of the outflows. The tube was shifted by the piezoelectric device, by which the cell was perfused with different temperatures. The positions of the tube were reversed after 1 s. The movements of the piezoelectric device (200 μm) were controlled by pClamp software so as to coincide with the voltage command. The driving voltages for the piezoelectric device were started and terminated with a finite slope to dampen the mechanical oscillations produced by the movements. This method allowed repeated brief applications of both warming and cooling jumps.

Double-barreled tube

The double-barreled tubes for the perfusing solutions were made of copper pipe (length, 100 mm; diameter, 1 mm) for better heat conduction. The surface of the copper pipe was silanized (Siliconise L-25; Nacalai Tesque, Inc.). A small Peltier device (5 × 5 mm; Miniature Module; Ferrotec Corp.) was mounted on a copper plate at the base of each tube. The two Peltier devices were controlled independently by a constant current source (PD18-10A; Regulated DC Power Supply; Kenwood). The pipes were insulated by tubing (Tygon) and were bundled in parallel with epoxy resin. A fine-fused silica tube coated with polyimide (MicroFil; WPI) was attached to the tip of the copper pipe to define a small outlet of fixed size (inner diameter of the tip, 250 μm). The temperatures of the outflow monitored by the ultrafine thermocouple reached

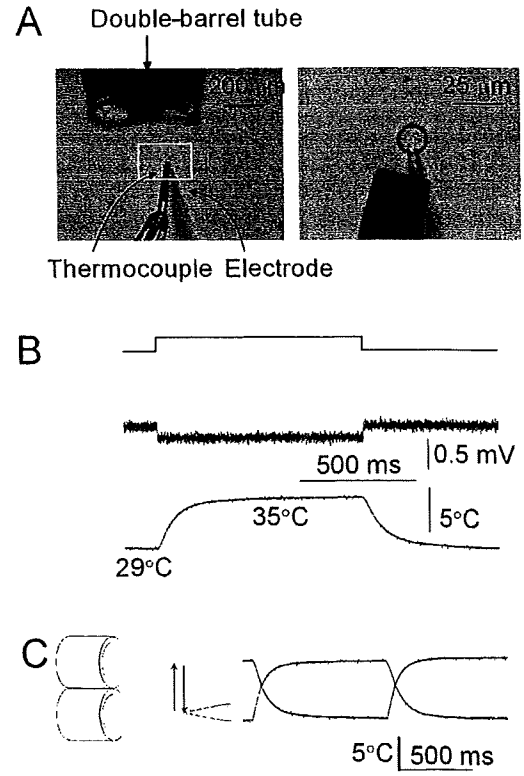

Figure 1. Temperature jump experiments. (A) The experimental setup. (Left) A photograph of the temperature pulse system. Solutions with different temperatures flowed from the double-barreled tube. A voltage-clamped microglial cell was placed close to one of the outflows. The piezoelectric device was driven by 5-V pulses, which were triggered by a program simultaneously controlling the membrane potential. (Right) An enlarged photograph for a patch-clamped cell and an ultrafine thermocouple located as close as 15 μm downstream of the cell. (B) Temperature measurements. (Top) The voltage drive for the piezoelectric device. (Middle) Temperature measured by a liquid junction potential using an open-tip electrode under current clamp mode. (Bottom) Temperature monitored by an ultrafine thermocouple. (C) Temperature measurements during the shift of the outflow from the double-barreled tube. Reversals of the shift motion and the responses of the thermocouple were recorded. The traces for 1-s pulses for reverse directions were mirror images of each other, indicating that the fast changes of temperature during a pulse were detected by the ultrafine thermocouple.

Published August 31, 2009

the steady state within a minute when the driving currents for the Peltier device were changed.

Evaluation of temperature changes

The local temperatures in the vicinity of the cell were monitored by an ultrafine thermocouple with a thermometer (BAT-12; Physitemp Instruments Inc.). The thermocouple with the tip size of 26 μm (ANBE SMT Ltd.) was insulated in a glass capillary with the fine tip exposed. The thermocouple was calibrated before use with a standard thermister.

Time courses of the temperature changes upon the jumps were monitored by the changes of the liquid junction potentials (Fig. 1 B, middle). An open-tip electrode filled with 3 M KCl was placed in the midst of the flow, and the liquid junction potentials were measured under the current clamp mode. Positive pressure was applied continually to the pipette to prevent the mixing of the solutions. The changes in temperature upon the shift of the flow were measured with a time constant of 0.9 ms.

The responses of the ultrafine thermocouple were evaluated under the temperature jump experiments. Output of the thermocouple is shown (Fig. 1 B, bottom trace), which was fitted by a single-exponential function with the time constant of ~70 ms. After a pulse, the temperature returned to the prepulse level within the error of 0.5%. To see whether the temperature signal from the thermocouple reached the steady state during a 1-s pulse, the sensor tip was placed in the outflows for minutes and the signal levels before and during a pulse were compared (Fig. 1 C, red trace). Conversely, the sensor tip was placed in the high temperature outflow for minutes and the temperature outflow was jumped to the low temperature for a second (Fig. 1 C, black trace). The responses to the shifts of the outflows in the opposite direction looked like mirror images of each other, indicating that the temperatures during the short jumps reached the steady-state values and were maintained there.

In addition to the changes in current amplitudes at different temperatures, the driving forces may be affected by several physicochemical factors. The temperature dependence of the Nernst potential and intracellular and extracellular pH changes by altered pK_a values for buffers were evaluated (see Appendix in detail). These factors develop instantaneously, but the theoretical prediction indicates that the contributions of these factors are negligible.

Evaluation of temperature dependence

The temperature coefficient for a 10° change in temperature, Q_{10}, is defined from current ratios as $I_{ratio}(\Delta T)^{10/\Delta T}$, where $I_{ratio}(\Delta T)$ is the temperature coefficient for an arbitrary temperature interval ΔT. Q_{10} as a function of the measured temperature was evaluated in several different ways. For the jump vector plot, a slope for each temperature jump vector was calculated. Q_{10} of the conductivity for the buffered solution was analyzed by the following method. Temperature-dependent conductivity was plotted and a slope was calculated by a linear fit of five neighboring data points. Slopes were obtained successively as the data points for evaluation were shifted. These slopes gave Q_{10} values at mean temperatures of five data points.

Resistivity pulse experiments

To estimate the access resistance, resistivity pulse experiments were performed in which the extracellular solution was changed to a solution with higher resistivity by use of a high concentration of sorbitol (Stojilkovic et al., 2003). The solution composition was 100 mM Mes, 105 mM NMDG, 90 mM aspartate, 1 mM $CaCl_2$, 1 mM $MgCl_2$, 50 μM DIDS, and 0.14–2 M sorbitol. The pH of the solutions was adjusted to 5.5 by CsOH, such that the pH of the extracellular and intracellular solution was symmetrical. The pipette solution was the same as in the previous experiments. The resistivities of the buffered solutions as a function of the sorbitol concentration and that of temperature were measured by a conductivity meter (DS-8M; HORIBA).

Proton currents were elicited by the depolarization pulses to +100 mV, and after reaching the steady state of the activation, the cells were exposed to the solution with high resistivity for short periods of time (the resistivity pulse method) (Ando et al., 2005). Current amplitudes immediately before and after a resistivity jump were measured. The ratios of the current amplitudes were evaluated as a function of the resistivities of the solutions. The relative resistivity of the channel to that of the total resistance was obtained.

All the algebraic calculations were performed using Mathematica (Wolfram Research Inc.), and the graphs were drawn using Origin (OriginLab Corporation). Data were expressed as mean ± SEM.

Online supplemental material

Fig. S1 provides reciprocal relationships of I_{ratio}s at the beginning and end of a pulse, which supports negligible contribution of the concentration polarization to the measured currents. Fig. S2 demonstrates all the experimental data points for temperature dependence in a three-dimensional plot. Fig. S3 shows discrepancies in temperature dependence measured by the temperature pulse method and by the earlier method measuring the steady-state current amplitudes. Figs. S1–S3 and supplemental text are available at http://www.jgp.org/cgi/content/full/jgp.200910213/DC1.

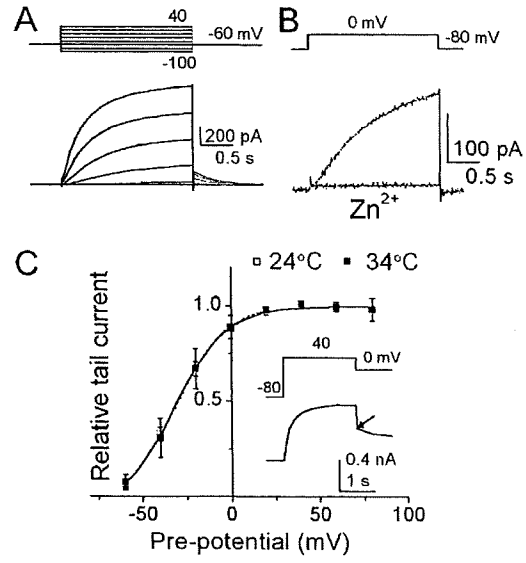

Figure 2. Proton channel currents. (A) Whole cell proton currents from a microglial cell. Voltage-dependent activation of the proton currents are shown. Currents were elicited by pulses from −100 to 40 mV. Inset represents the voltage protocol. (B) Block of the proton currents by 100 μM of extracellular Zn^{2+}. (C) Steady-state gating curves (*G-V* curve) of proton channel and its temperature dependence. The current amplitudes at the peak of the tail currents were plotted as a function of preceding voltages and were normalized. *G-V* curves were obtained from six cells at 24 and 34°C. The curves were fitted by the Boltzmann function. The $V_{1/2}$ values were −32.2 and −30.2 mV for 24 and 34°C. Inset shows a representative current trace for depolarizing pulse to +40 mV, followed by repolarization to 0 mV. The arrow indicates the peak of tail current.

Published August 31, 2009

RESULTS

Proton channels of microglial cells

Proton currents were recorded from microglial cells in the whole cell voltage-clamped configuration. In the asymmetric pH condition (pH_i/pH_o, 5.5/7.3), depolarizing pulses elicited a slowly activating outward current, the time course of which was accelerated with further depolarization (Fig. 2 A) (Morihata et al., 2000b). This current was inhibited by a proton channel blocker, Zn^{2+} (Mahaut-Smith, 1989), indicating negligible contributions from other endogenous channels (Fig. 2 B).

To examine the temperature dependence of the steady-state gating, depolarizing pulses to various membrane potentials were applied and the tail currents at 0 mV were recorded (see Fig. 4 C, inset). The normalized peak amplitudes of the tail currents as a function of the depolarizing potentials were plotted (*G-V* curve; Fig. 2 C). The two curves at different temperatures overlapped; thus, the steady-state gating of the proton channel was not temperature dependent.

Cytosolic protons are depleted slowly

Before studying the temperature dependence of proton permeation through the channel, factors affecting the driving force upon temperature change were examined. Proton effluxes should deplete cytosolic protons (cytosolic depletion), and the degree of the depletion and its time course were evaluated. Proton effluxes were elicited by repeated application of depolarizing pulses that were prolonged successively (Fig. 3 A). A ramp potential was applied at the end of a depolarization pulse to give *I-V* curves (Fig. 3 B). The reversal potentials (V_{rev}s) shifted notably toward the positive direction for longer depolarizations. Because the bath concentrations of protons were held constant by continual perfusion, the positive shifts of V_{rev} indicate decreases in the intracellular concentrations of protons.

The proton currents sometimes decayed gradually after reaching the peak level of activation (Fig. 3 C). This is called current droop. In parallel to the current droop, V_{rev} shifted slowly within the time range of seconds (Fig. 3 D, ■; 24°C). When the temperature was raised to 34°C, the degrees and speeds of the V_{rev} shift were dramatically enhanced (Fig. 3 D, ○), although the time range was still of the order of seconds.

Evaluation of the temperature pulse method

Temperature dependence of proton currents was examined by measuring the immediate changes in current amplitude upon temperature jumps (see Materials and methods). To verify that the fast temperature changes were sensed by the channels in cell membrane, the time courses of whole cell currents upon a temperature pulse were examined. The thermocouple signals displayed reproducible changes for the repetitive temperature pulses (Fig. 4, middle). When a pulse was applied early during the gating activation, a small jump of the current was followed by accelerated gating activation during the pulse (Fig. 4, bottom, red arrows). As the onset of the temperature pulse on top of the depolarization pulse was delayed, the instantaneous changes in the current traces predominated, and these were followed by residual activation. These observations, of the current jumps superimposed on temperature jumps and accelerated activation gating during a temperature pulse, were consistent

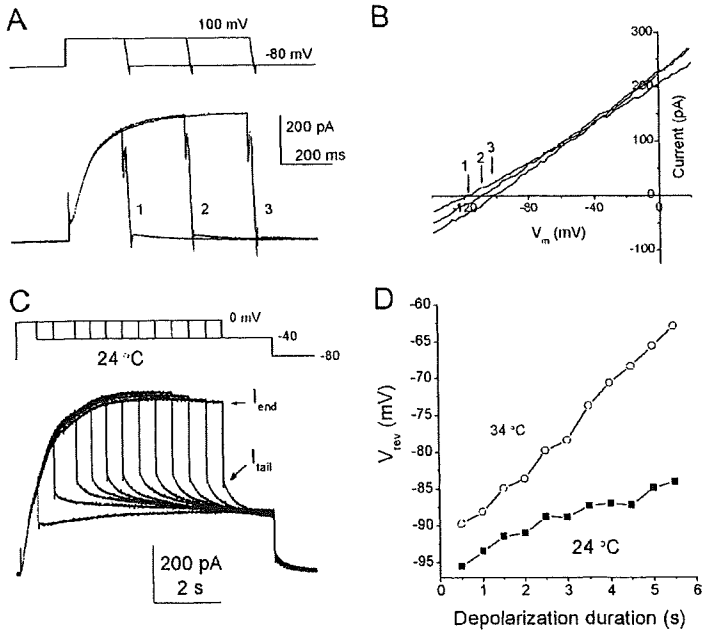

Figure 3. Changes in the intracellular pH after proton flux. (A) Current traces for depolarization pulses, followed by the ramp potential from 100 to −100 mV. (B) The *I-V* curves for depolarization pulses of different durations. The V_{rev} is indicated by arrows, and the number represents current traces shown in A. V_{rev} shifted toward the depolarization potential as the depolarization pulse was prolonged. (C) Current traces with droop. As the depolarization pulses were prolonged, current amplitudes reached nearly steady state and slightly decayed. The tail currents were measured at −40 mV. Current amplitudes at the end of the depolarization pulse (I_{end}) and those at the peak of tail currents (I_{tail}) are indicated by arrows. (D) Time courses of the shifts for V_{rev}. V_{rev}s were estimated from a current ratio (I_{tail}/I_{end}). Shift of V_{rev} for the higher temperature was accelerated.

Published August 31, 2009

with the expected responses to stepwise changes in temperature, and suggest that the cellular temperature under whole cell recordings changed rapidly.

During a temperature pulse, the temperature sensed by the channel molecule in situ was evaluated. Because the gating of proton channels exhibits a high sensitivity to temperature (Byerly and Suen, 1989; Kuno et al., 1997; DeCoursey and Cherny, 1998), the accelerated gating kinetics upon heating pulses were used for the evaluation. First, the activation time courses of proton currents at a steady-state bath temperature, elicited by depolarizing pulses to 0 mV, were fitted with a triple-exponential function, and the time constants were plotted as a function of temperatures measured in the vicinity of the cell (Fig. 5, filled symbols). Then, the warming temperature pulses were applied during the gating activation. When the temperature pulses were applied after faster activation components were nearly completed, the accelerated time courses for the residual activation during temperature pulses were fitted by a single-exponential function. These time constants (Fig. 5, open symbols) were superimposed on the plot of time constants observed at the steady-state bath temperature. The data points from the temperature pulses overlapped onto the distribution of the slowest components of the activation time constants. The Q_{10} for the activation time constant measured under the pulse method was similar to that measured when the entire bath was temperature controlled (5.6 ± 0.5; $n = 33$). These data indicate that the temperatures applied to the channel molecules on the cell were monitored successfully by the thermocouple adjacent to the cell.

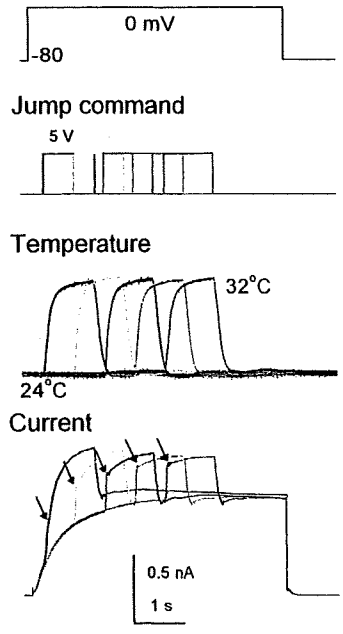

Figure 4. Current responses to temperature pulses. A patch-clamped cell at an intracellular pH of 5.5 was placed in the midst of a laminar outflow, and an ultrafine thermocouple was located downstream of the cell within 15 μm. Proton currents were elicited by depolarizing pulses to 0 mV (top; pulse duration was 4 s), during which a temperature pulse of 1 s (from 24 to 32°C; ΔT = 8°C) was applied at different phases of the gating activation. The pulse command indicates the driving voltages to the piezoelectric device. The thermocouple signals displayed reproducible changes for the repetitive temperature pulses. Ensemble current traces with responses to temperature pulses elicited at different timings of the activation are superimposed.

Temperature pulse experiments under various conditions

Temperature pulses applied during the steady state of gating activation produced clear stepwise changes in the currents upon both the onset and termination of the pulses (Fig. 6 A). Upon the return to the prepulse temperature, the amplitudes of the currents reverted to those before the pulse, confirming that the open-state probability had not been changed during a pulse. Pulses with various magnitudes of ΔT either warming or cooling were applied at various temperatures (pre-jump temperature; Fig. 6 A, a, c, and f, and b, d, and e). At low temperatures (Fig. 6 A, e and f), long (>8 s) depolarization pulses were required for the gating activation to reach the steady state. At −100 mV, which is outside of the activation range for the gating, temperature jumps produced negligible changes in current amplitude (Fig. 6 B).

The ratio of current amplitudes, I_{ratio}, as an index for temperature dependence

To evaluate the temperature dependence of current amplitudes immediately before and after a temperature

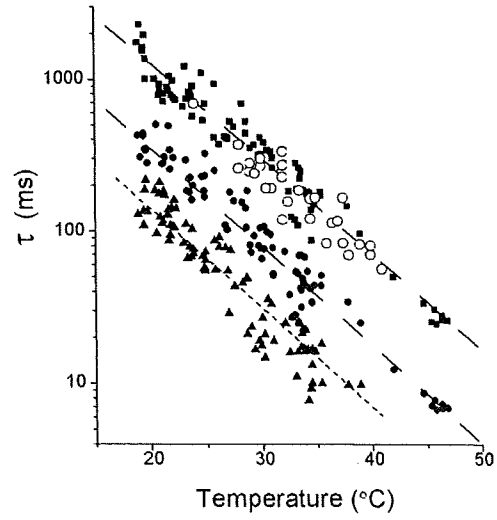

Figure 5. Temperature-dependent time constants for the activation gating. The activating currents at 0 mV were fitted by a triple-exponential function. Temperature pulses were applied after the faster activation phases were nearly completed. Current traces during temperature pulses were fitted with a single exponential. Three time constants at various temperatures (filled symbols) and the time constant during the pulse (open symbols) are shown. The data were obtained from a single cell.

Published August 31, 2009

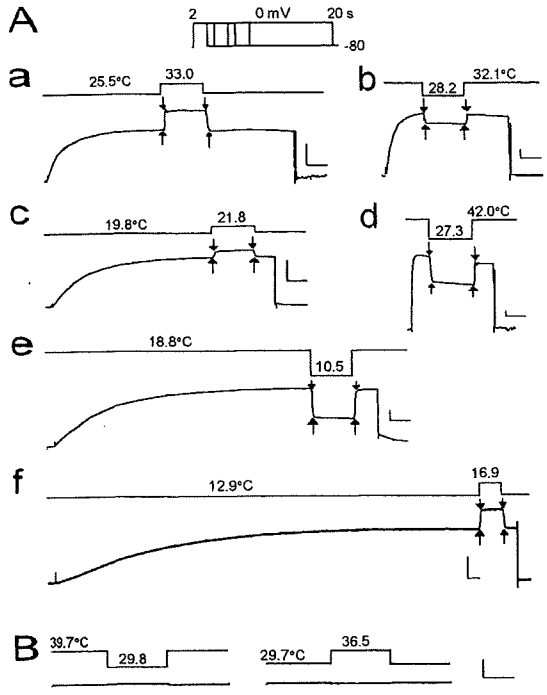

Figure 6. Responses of the proton currents to temperature pulses (pH_i/pH_o, 5.5/7.3). (A) Proton currents were elicited by depolarizing steps to 0 mV (inset; the voltage command with the holding potential of −80 mV). Temperature pulses (blue lines; duration, 1 s) were applied during the steady state of the gating activation. Current amplitudes were measured immediately before and after the onset (red arrows) and termination (blue arrows) of the pulses. The depolarizing pulses were followed by hyperpolarizing ramps (20 ms), and the outward tail currents were not obvious in these traces. (B) Temperature pulses were applied at the hyperpolarizing potential of −100 mV.

jump, the current amplitudes for each jump were plotted as a function of pre-jump and jump temperatures, and the points were connected to draw a vector (jump vector; Fig. 7 A). The direction of the vectors indicates whether the pulse was cooling (down) or warming (up). Plots of the vectors from six different cells over a wide range of temperatures with variably sized ΔTs and directions (warming or cooling) showed a general trend of vector flow.

Jump vectors were examined for different membrane potentials (Fig. 7 B). Temperature jumps of a fixed ΔT (from 16.7 to 12.7°C) were applied during variable depolarizing steps. Each column of arrows represents jump vectors from a cell. The slopes of the vectors on the logarithmic scale were almost identical, even though the current amplitudes at different membrane potentials differed considerably.

The ratios of the current amplitudes were calculated from the vectors (current ratio; $I_{ratio} = I_{jump}/I_{pre\text{-}jump}$) and were plotted at different membrane potentials (Fig. 7 C), where the ΔTs were set differently for cells. The I_{ratio}s were distributed nearly horizontally, indicating that the I_{ratio} was not affected by the current amplitudes.

Temperature dependence of Q_{10} over a wide temperature range

A plot of the values of I_{ratio}s as a function of ΔTs shows nearly linear relationships. I_{ratio}s were measured from many cells over a wide range of pre-jump temperatures (4–49°C) and ΔTs (±15°C) (see three-dimensional plot in Fig. S2). I_{ratio}–ΔT relationships are shown for different ranges of pre-jump temperatures (Fig. 8). Linear relationships hold at relatively narrow ranges of pre-jump

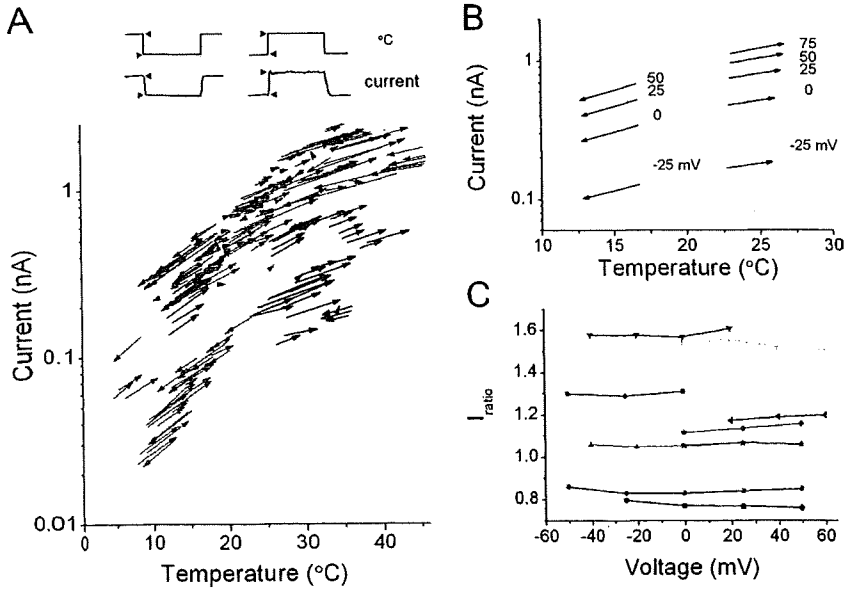

Figure 7. The jump vector plot and current ratios. (A) The jump vector plot over a wide temperature range (pH_i/pH_o, 5.5/7.3). Current amplitudes immediately before and after a temperature jump (arrow heads) were plotted for pre-jump (tail of arrows) and jump (head of arrows) temperatures. Arrows were obtained from six different cells. Each colored arrow represents data from a single cell. A depolarization pulse of 0 mV was applied. Note that the axis for the current amplitude is logarithmic. (B) The jump vector plots at different membrane potentials ranging from −25 to +75 mV. Arrows from different membrane potentials in two different cells (left column, cool-down jump; right column, heat-up jump) are shown. (C) I_{ratio}s at different membrane potentials. A set of I_{ratio}s from nine cells is shown. For each cell ΔT was fixed.

Published August 31, 2009

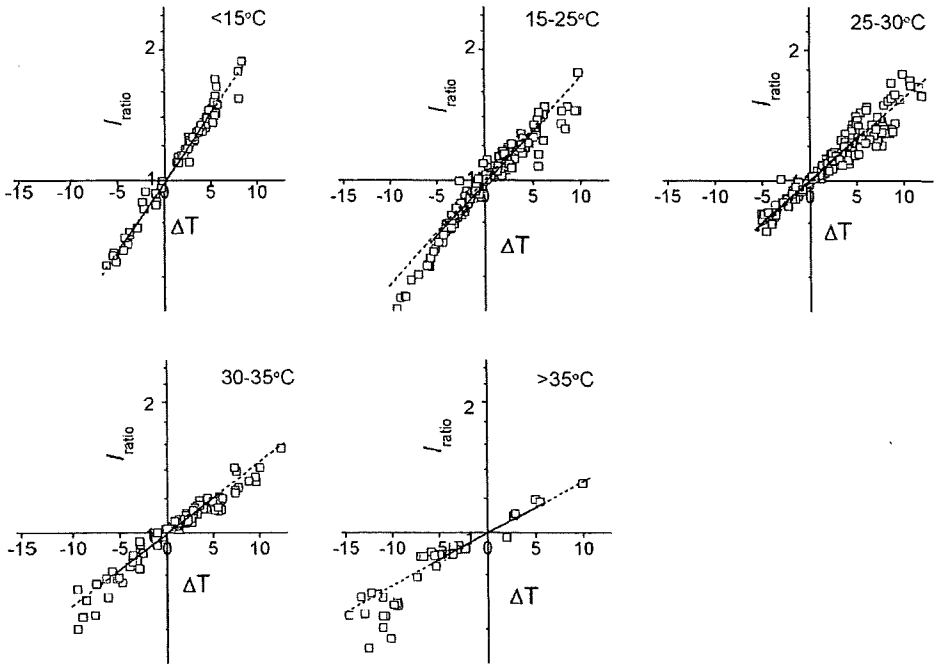

Figure 8. Temperature dependencies of I_{ratio}s. I_{ratio} as a function of ΔT for different pre-jump temperatures. The data points were fitted by a linear function, and the Q_{10} values were obtained from the slopes. Solid lines were fitted to the data with the absolute ΔT value <5°, and the broken lines are the extrapolations. Q_{10} values were 1.98 < 15°C, 1.79 for 15 ≤ T < 25°C, 1.60 for 25 ≤ T < 30°C, 1.46 for 30 ≤ T < 35°C, and 1.32 > 35°C.

temperatures. The slope is a measure of temperature dependence of proton currents, and the Q_{10} value was calculated (see Materials and methods). Fig. 8 demonstrates that the Q_{10} value decreased significantly over a measured temperature range. A similar relation was observed at pH 6.2 (not depicted).

To obtain thermodynamic clues for this phenomenon, the jump vector data were expressed as an Arrhenius plot, in which pairs of current amplitudes for each temperature jump were plotted against $1/T$ (T, the absolute temperature; Fig. 9). The slopes of the arrows became steeper as the temperature was decreased (toward the right of the horizontal axis) and, overall, the arrows indicate a trend that is curved (convex). A curved Arrhenius plot is generally considered to indicate the presence of multiple processes with different underlying natures (Gutfreund, 1995; Fersht, 1999).

To quantify the temperature dependence, the mean Q_{10} values were plotted as a function of temperature (Fig. 10). The Q_{10} value of 2.2 at 10°C decreased monotonically as the temperature was increased and reached 1.3 at 40°C. The strong temperature dependence of the Q_{10} values has not been reported in earlier studies, at least for the permeation of channels.

The rate theory (Kramers, 1940) was applied to express proton permeation at different temperatures with thermodynamic parameters (see Eq. A1). Q_{10} as a function of T can be expressed as

$$Q_{10}(T) = Exp\left[10\left(\frac{\Delta H^{\ddagger}}{RT^2} + \frac{1}{T}\right)\right], \quad (2)$$

where $\Delta H^{\ddagger}$ represents the activation enthalpy. This equation demonstrates that Q_{10} value changes at different temperatures, the extent of which can be estimated. The changes of Q_{10} at constant $\Delta H^{\ddagger}$ values are shown in Fig. 10 (dotted lines, iso-enthalpy lines). As expected, the experimentally obtained Q_{10}s did not align on the

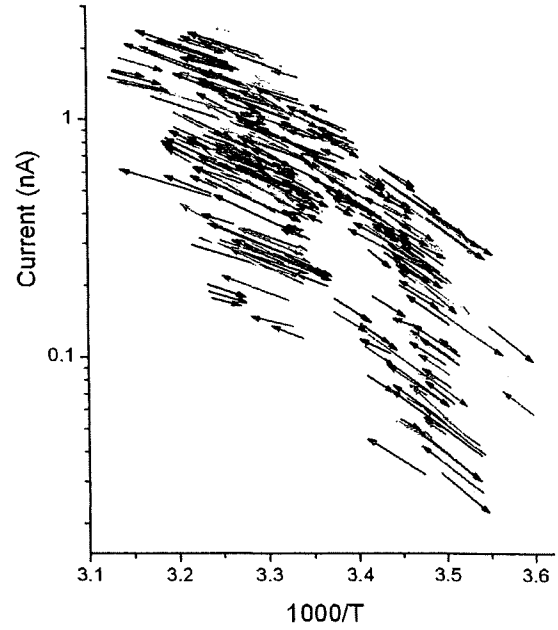

Figure 9. An Arrhenius plot for the proton permeation process through the voltage-gated proton channel. Each arrow represents data for the onset of a temperature pulse.

Published August 31, 2009

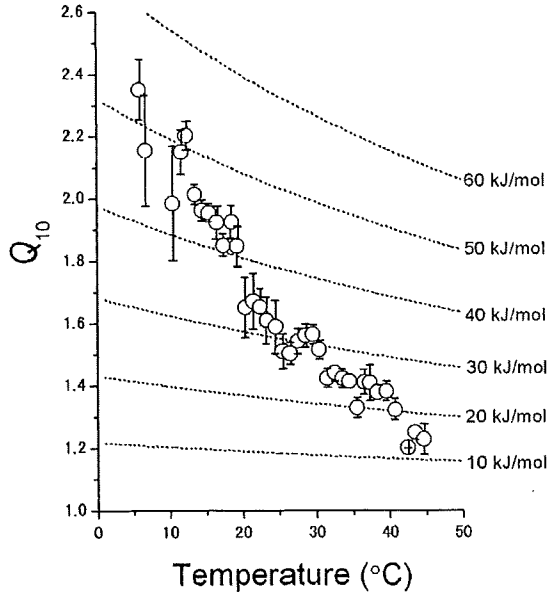

Figure 10. Temperature dependence of Q_{10} values. Q_{10} values were calculated from the data of temperature jump experiments. A set of dotted lines indicates temperature-dependent Q_{10} values for fixed activation enthalpy (iso-enthalpy line).

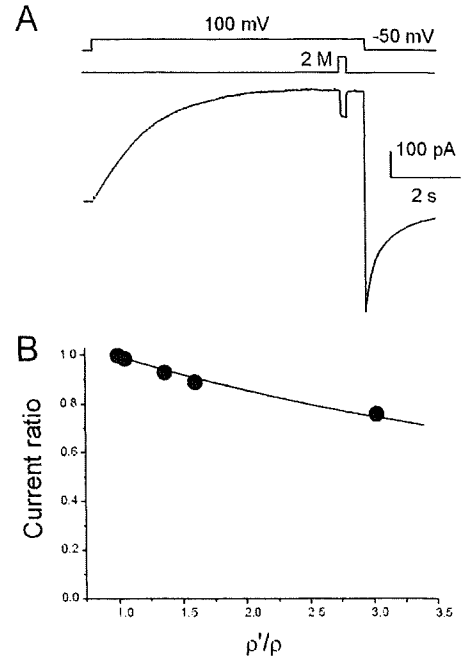

Figure 11. Estimation of the access resistance. (A) Current traces for the resistivity pulse experiments. The pHs were symmetrical (pH, 5.5), and the temperature was 23°C. A patch-clamped cell was exposed briefly to a solution containing 2 M sorbitol. The current amplitudes were measured immediately before and after a jump. (B) Current ratios as a function of the relative resistivity of the solutions. ρ is the resistivity of the bathing solution, and ρ' is the resistivity of the pulse solution. The data were fitted by Eq. A10. The ratio of the resistances (R_{AR}/R_{Ch}) was 0.25.

iso-enthalpy lines, but cut across them. What is the underlying mechanism for the strong temperature dependence of Q_{10}? Multiple processes with different thermodynamic natures are involved in the measured currents. From the theoretical prediction, one possible candidate underlying the observations is the access resistance that develops instantaneously ($<10^{-10}$ s; see Experimental strategy and Appendix), and hence its contribution to the measured current even with the rapid temperature change cannot be eliminated.

Estimation of the access resistance

Direct measurements of the access resistance (R_{AR}) are impossible, but the relative contribution of R_{AR} to the measured current (or R_{total}) can be estimated. Hall's equation indicates that R_{AR} changes with the resistivity of the bathing solution (see Eq. A7). Therefore, if a cell is perfused with a different resistivity solution, changes in the external R_{AR} lead to changes in R_{total}. Analyses of an equivalent electrical circuit having R_{Ch} (the channel resistance) and R_{AR} in series (see Appendix) demonstrated that the ratio of R_{total} in two different resistivity solutions gives the ratio of R_{AR} and R_{Ch} (see Eq. A8). Here, an experimental method for evaluating R_{AR}/R_{Ch} was developed (the resistivity pulse method [R pulse method]). Proton currents were elicited by depolarization pulses to +100 mV. After reaching steady-state activation, the cells were exposed to the high resistivity solution for a short period of time (250 ms; Fig. 11 A; see Materials and methods) (Ando et al., 2005), and current amplitudes before and after a resistivity jump were measured. In these experiments, solutions on both sides of the membrane were set symmetrically (pH, 5.5); hence, R_{AR}s on the intracellular and extracellular sides were assumed to be identical.

The current trace demonstrated, surprisingly, large decreases in amplitudes upon exposure to a high resistivity solution, suggesting a large contribution of the access resistance. The current ratios were plotted as a function of the relative resistivities of the solutions (Fig. 11 B). Proton currents decreased gradually as the resistivity of the external solution was increased. The R_{Ch}/R_{AR}s were obtained through fitting the current ratio of Eq. A11 to the data. The value of R_{Ch}/R_{AR} was 3.8 and that of R_{Ch}/R_{total} was 0.66 at 23°C. A notable contribution of R_{AR} to R_{total} suggests that the observed Q_{10} values do not solely represent temperature dependence of the channel per se, but represent a weighted average for those of the channel and the access resistance. Therefore, we redefine here the observed Q_{10} as the apparent Q_{10} (Q_{10}^{app}). It should be noted that R_{Ch}/R_{AR} is not constant over the temperature range because the temperature dependencies of the channel and access resistances differ. Then it is likely that the strong temperature dependence of Q_{10}^{app} is produced by the relative contribution of Q_{10} for the

Published August 31, 2009

access resistance (Q_{10}^{AR}) and for the channel (Q_{10}^{Ch}), which varies as the temperature changes.

The Q_{10}^{Ch} was decomposed from Q_{10}^{app} by the series resistance model (see Appendix). Each resistance (R_{Ch} and R_{AR}) can be characterized by its own thermodynamic parameters, such as the activation enthalpy and entropy. An equation was derived for the temperature dependence of the Q_{10}^{app} values as a function of the thermodynamic parameters for the channel and access resistance (see Eq. A14). In this equation, temperature dependence of R_{AR} (Q_{10}^{AR}) can be represented by of the buffer solution (Hall's equation) (Hall, 1975), which was evaluated by measuring the conductivity of the buffered solution at different temperatures (Fig. 12 A). The Q_{10}^{AR} value was 1.2 at 25°C and decreased slightly at higher temperatures (Fig. 12 B). If the thermodynamic parameters for the channel, in addition to the access resistance, would be given, the series resistance model would provide temperature dependencies of observable currents and Q_{10}^{app}.

Conversely, now that data for temperature dependency of Q_{10}^{app} and the thermodynamic parameters of the access resistance are available (data points in Fig. 12 B), thermodynamic parameters for the channel were obtained through optimizing the parameter as to fit the calculated Q_{10}^{app} line to the Q_{10}^{app} data. The blue line in Fig. 12 shows the estimate for the temperature dependence of Q_{10}^{Ch} (an iso-enthalpy line). In this figure, strong temperature dependence of Q_{10}^{app} was decomposed into Q_{10}^{AR} and Q_{10}^{Ch}. Finally, the activation enthalpy ($\Delta H^{\ddagger}$) for proton permeation through the channel per se was determined to be 64 kJ/mol. (Similar values of thermodynamic parameters for the channel [or Q_{10}^{Ch}] were obtained through fitting procedures using data of I_{ratio}s at different temperatures and ΔTs; Fig. S2).

DISCUSSION

The temperature dependencies of proton permeation through the voltage-gated proton channel per se (Q_{10}^{Ch}) are masked by many layers of phenomena, and the aim of this study was to isolate Q_{10}^{Ch}. By applying temperature pulse methods, the overlying factors, such as the changes in the number of active channels and the driving forces of proton permeation, were successfully excluded. The measured Q_{10}, however, exhibited unexpectedly high temperature dependence, which cannot be accounted for by a simple physical process (hence named Q_{10}^{app}). We suspected that Q_{10}^{app} represents a mixture of multiple processes with different temperature dependencies. The novel resistivity pulse experiments allowed the quantitative evaluation of the access resistance (R_{AR}) and revealed significant contribution of R_{AR}. Finally, we extracted Q_{10}^{Ch}, attained for the first time, and the value was 2.5 at room temperature and the activation enthalpy was 64 kJ/mol. These thermodynamic features will be discussed for the underlying mechanisms of proton permeation through the voltage-gated proton channel.

Verification of the temperature pulse method

The T pulse method is characterized by its rapid change of temperature, which minimizes the contributions of the slowly developing events, i.e., proton depletion and concentration polarization. The validity of the T pulse method was demonstrated in various ways, as follows. The stepwise changes in temperature were confirmed by the rectangular shapes of the measured liquid junction potentials (Fig. 1 B) and of the proton currents themselves (Figs. 8–10). Throughout the experiment, the temperature in the vicinity of the cell was monitored

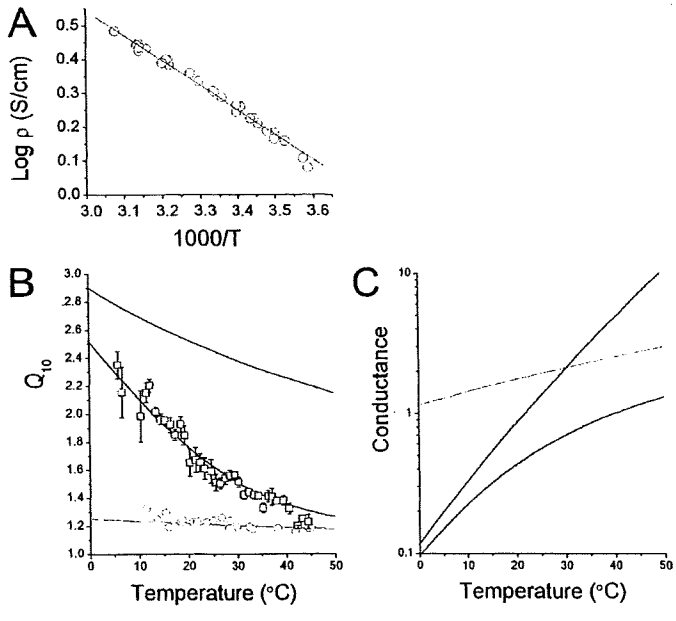

Figure 12. Decomposition of apparent Q_{10} (Q_{10}^{app}). (A) Measured conductance (ρ) for the Mes-buffered solution represented as the Arrhenius plot. The $\Delta H^{\ddagger}$ value was 14.0 kJ/mol, and the preexponential factor was 556.7. (B) Temperature dependencies of Q_{10}^{AR} (green symbols and line), Q_{10}^{Ch} (blue), and Q_{10}^{app} (red symbols and line) values. Q_{10}^{AR}s were calculated from the data for A (see Materials and methods). A $\Delta H^{\ddagger}$ value of 12.5 kJ/mol was obtained by fitting to the Q_{10}^{AR} values. $\Delta S^{\ddagger}$ was set to zero. Using $\Delta H^{\ddagger}$ and $\Delta S^{\ddagger}$ values for the access resistance, the values of $\Delta H^{\ddagger}$ and $\Delta S^{\ddagger}$ for the channel were estimated through fitting Eq. A10 to Q_{10}^{app} data. $\Delta H^{\ddagger}$, $\Delta S^{\ddagger}$, and ω_C for the channel were 63.7 kJ/mol, 8.49 J/mol/T, and 0.0115. Q_{10}^{Ch} (blue line) was drawn using the above fitted parameters. (C) Temperature dependencies of conductances for access resistance (green), channel (blue), and total (red) values. Conductances were calculated using the thermodynamic parameters.

Published August 31, 2009

with an ultrafine thermocouple (Fig. 1), which demonstrated that ambient temperature of the channels in situ (on the plasma membrane) was well controlled by the pulse method (see Fig. 7). These results indicate that the temperature pulse method readily provides variable up-and-down temperature jumps to whole cell clamped cells within a few milliseconds in a reproducible and accurate manner.

The I_{ratio} introduced here as a robust measure of temperature dependence served for calculating Q_{10}^{app}. Q_{10}^{app}s were evaluated under various experimental conditions: at different intracellular pHs, at different membrane potentials (Fig. 7), and in the presence and absence of droop.

Q_{10} for proton permeation per se extracted from the temperature-dependent Q_{10}^{app}

A key finding of the present study was that the Q_{10}^{app} values changed significantly over a wide temperature range (Fig. 10). Generally, the Q_{10} value should change somewhat. In fact, simple physical processes, such as proton-transfer processes through the access region and the channel pore, can be described by the rate theory (see Eq. A1), and the temperature dependence of the pre-exponential factor for the rate equation leads to slight temperature dependence of Q_{10}, which follows the isoenthalpy line (Fig. 10). The large changes in the Q_{10}^{app} values over ~1 unit between 4 and 49°C suggest that multiple processes with different temperature dependences are involved.

A seminal paper by Decker and Levitt (1988) led us to examine the contribution of access resistance to the total proton current in the presence of a high concentration buffer. The *R* pulse method revealed unexpectedly large changes in current amplitudes upon exposure to the high resistivity solution, suggesting a significant contribution of the access resistance to the measured current. A simple model for resistances in series of the channel and access regions (the series resistance model) was adopted for quantitative evaluation, and the R_{Ch}/R_{total} ratio was estimated to be 0.66 at room temperature. This value makes evident that the contribution of the access resistance to the measured current was important.

The series resistance model demonstrates that if thermodynamic parameters for the channel and the access region are given, the temperature-dependent Q_{10}^{app} can be readily calculated. The thermodynamic parameters for the access resistance were estimated from that of the resistivity of the buffered solution (Fig. 12 B, green line) (Hall, 1975). Now that Q_{10}^{app} and Q_{10}^{AR} are given, Q_{10}^{Ch} and its thermodynamic parameters can be estimated through the fitting procedure.

Fig. 12 B demonstrates graphically how the strong temperature dependency of Q_{10}^{app} is decomposed into Q_{10}^{Ch} and Q_{10}^{AR}. At low temperature the Q_{10}^{Ch} predominates, and at high temperature the Q_{10}^{AR} predominates. Q_{10}^{app} traverses from Q_{10}^{Ch} to Q_{10}^{AR} through the measured temperature range. The activation enthalpy for proton permeation through the channel was finally extracted. (These thermodynamic parameters were also obtained from direct fit to the I_{ratio} data; Fig. S2.) The Q_{10}^{Ch} value was 2.5 at room temperature, and the $\Delta H^{\ddagger}$ value was 64 kJ/mol.

Before discussing the implication of the activation enthalpy for the proton permeation, the physiological relevance of Q_{10}^{app} will be discussed.

The Q_{10}^{app} under physiological conditions

The Q_{10}^{app} values obtained here were smaller than the Q_{10} of earlier reports (5.3 ≤ 20°C and 2.8 > 20°C) (DeCoursey and Cherny, 1998), which might be overestimates because they included the contribution of changes in the numbers of activatable channels at different temperatures (Fig. S3). In Fig. 12 C, the temperature-dependent conductance was decomposed into the conductance for the channel (blue line) and that for the access resistance (green line). This figure was drawn using the thermodynamic parameters, demonstrating the relative contributions. The temperature-dependent conductances of the channel and the access resistance form asymptotes for the observed conductance (Fig. 12 C, red line). These parameters gave the ratio R_{Ch}/R_{total} as 0.46 at 23°C, which is in rough agreement with the ratio predicted from the *R* pulse method. Because the temperature dependence of the channel conductance is much higher than that of access resistance, the channel conductance overwhelmed that of the access resistance and the whole process became diffusion limited above the crossing point of ~30°C. In physiological conditions, in which the buffer concentrations are much lower than in the present experimental conditions, the temperature dependence of the voltage-gated proton channel, Q_{10}^{app}, is apparently governed by diffusion-limited processes and is almost indistinguishable from those of other types of ion channels.

Mechanisms for proton-selective permeation

The temperature dependence of proton permeation has been studied systematically only for the gramicidin A (gA) channel, which is proton conducting, but not proton selective (Andersen, 1984; Heinemann and Sigworth, 1989; Oiki et al., 1995; Koeppe and Anderson, 1996). Over a wide temperature range (Chernyshev and Cukierman, 2002), the Q_{10} values were nearly constant (Cukierman, 2000) and the $\Delta H^{\ddagger}$ values for proton permeation through most gA channels were 10–20 kJ/mol (Bamberg and Läuger, 1974; Akeson and Deamer, 1991; Chernyshev and Cukierman, 2002). These values are similar to those for proton diffusion in an aqueous solution, in which the Grotthuss mechanism predominates (Eigen, 1964; Agmon, 1995; Day et al., 2000; Limbach et al., 2006), and are in general agreement with the activation enthalpy for the buffered diffusion (Fig. 12 A). However,

Published August 31, 2009

it has been reported that the contribution of the access resistance to the recorded single-channel current is significant for proton permeation through the gA channel (Decker and Levitt, 1988; Cukierman, 2000; Schumaker et al., 2000; Schumaker, 2003; Braun-Sand et al., 2005). Therefore, the measured temperature dependence of earlier studies for the gA channel may be governed largely by the access resistance, similar to the voltage-gated proton channel. In fact, breaks in linearity or curved Arrhenius plots have been reported for gA channels (Chernyshev and Cukierman, 2002). The lower Q_{10} may represent the diffusion-limited ion access, and the higher Q_{10} (>30 kJ/mol) could represent the inherent proton permeation process.

The voltage-gated proton channel exhibits nearly perfect proton selectivity compared with the gA channels. We estimated the activation enthalpy of proton permeation through the channel to be 64 kJ/mol. This is essentially the first quantitative evaluation of a thermodynamic parameter for proton permeation through proton-selective channels. What is the underlying mechanism of the $\Delta H^{\ddagger}$ value for the proton permeation? Quantitative comparison of the present $\Delta H^{\ddagger}$ value with those of other types of channels must be reserved until the genuine $\Delta H^{\ddagger}$ values without effect of the access resistance would become available for other types of channels. Still, we anticipate that $\Delta H^{\ddagger}$ for the proton channel is significantly higher than for the gA channel, and a gap between the $\Delta H^{\ddagger}$ value of the proton channel and gA channels cannot be accounted for by simple modifications of the proton jump mechanism through a single-file pore. We present here a hypothetical mechanism for proton-selective permeation: A proton-selective site(s) should exist along a water-filled pore, and its configuration needs to be rearranged upon proton transfer, which would account for the additional cost of $\Delta H^{\ddagger}$ for the proton permeation. The mechanism of proton permeation through the molecular candidate of the voltage-gated proton channels (Ramsey et al., 2006; Sasaki et al., 2006; DeCoursey, 2008) and other proton-selective pores in the voltage sensor domain of potassium channels (Starace and Bezanilla, 2004) has not been studied. However, given the structural elements that the candidates possess, such as water crevices toward protonation sites, our hypothetical mechanism is compatible with those that the candidates may exhibit. Involvement of local structural changes during rearrangement of proton-accepting histidine residues may account for the observed activation enthalpy. Those are thermodynamic aspects of experimental evidence supporting the candidate molecule as the molecular entity of the voltage-gated proton channel.

Here, we conclude the temperature dependence of the voltage-gated proton channel. Q_{10}^{app} is a measure that represents the overall nature of proton permeation, including the access resistance. The value characterizes apparent behavior of the proton channel under physiological conditions and is almost indistinguishable from that for other types of channels (Hoffmann and Dionne, 1983; Urry et al., 1984; Grygorczyk, 1987; Miller et al., 1988; Sitsapesan et al., 1991; Milburn et al., 1995; Hille, 2001; Chernyshev and Cukierman, 2002). On the other hand, Q_{10}^{Ch} is a measure to characterize the proton permeation in the channel per se, and we have proposed an underlying mechanism of proton-selective permeation. These thermodynamic clues are prerequisite to advance our understanding of the mechanism of action for proton-selective permeation.

APPENDIX

Local proton concentration

In the presence of buffer, the concentration polarization is confined to a limited space, which otherwise extends farther from the membrane. Zifarelli et al. (2008) simulated the concentration profile of protons near the membrane. Their numerical evaluation showed that if the flux of protons is constant, the concentration polarization develops relatively slowly over a time range of several tens to hundreds of milliseconds. For example, the pH at the outer vicinity of the membrane decreased by 1.3 U in the presence of buffer concentration as low as 0.1 mM after 5 s of a proton efflux of 500 pA. This local proton accumulation decreased to a ΔpH of 0.07 U when the buffer concentration was increased to 2 mM. Following the reported method, we simulated the local accumulation when the buffer concentration was increased to 100 mM (our experimental condition). The ΔpH was only 0.0013 U at the vicinity of the membrane. The time course of the development was fitted by a double-exponential function, and the smaller time constant was ~60 ms. The slow development and attenuation of the concentration polarization in the concentrated buffer were used in the experimental strategy.

Temperature-dependent Q_{10}

The rate constant for the proton permeation was expressed in Kramers' theory (Kramers, 1940; Hänggi et al., 1990; Berry et al., 2000):

$$k(T) = \frac{\omega_A \omega_C}{2\pi\zeta} Exp\left[-\frac{\Delta H^{\ddagger} - T\Delta S^{\ddagger}}{RT}\right], \quad \text{(A1)}$$

where the preexponential factor can be expressed as:

$$\frac{\omega_A \omega_C}{2\pi\zeta} = \frac{\omega_C}{\zeta}\frac{\omega_A}{2\pi} = \frac{\omega_C}{\zeta}\frac{k_B T}{h}. \quad \text{(A2)}$$

In these equations, ζ is the friction coefficient, ω_C is the characteristic frequency, h is the Planck constant, R is the gas constant, and k_B is the Boltzmann constant.

Published August 31, 2009

This equation for condensed systems is valid in the limit of large friction. The temperature dependence for the friction coefficient is:

$$\zeta(T) = \frac{1}{aExp[-b/T]}. \quad \text{(A3)}$$

With this relation, the Kramers' equation becomes

$$k(T) = a\omega_C \frac{k_B T}{h} Exp\left[-\frac{\Delta H_{Ch}^{\ddagger}}{RT} - \frac{b}{T} + \frac{\Delta S_{Ch}^{\ddagger}}{R}\right], \quad \text{(A4)}$$

where $\Delta H_{Ch}^{\ddagger}$ is the activation enthalpy and $\Delta S_{Ch}^{\ddagger}$ is the activation entropy. Here, $\Delta H_{Ch}^{\ddagger}$ and b were lumped together as $\Delta H_{Ch}'^{\ddagger}$ ($=\Delta H_{Ch}^{\ddagger} + bR$) because $\zeta(T)$ and its temperature dependence cannot be obtained unequivocally. Also, a and ω_C were collected as ω_C' ($=a\omega_C$). Then,

$$k(T) = \omega_C' \frac{k_B T}{h} Exp\left[-\frac{\Delta H_{Ch'}^{\ddagger}}{RT} + \frac{\Delta S^{\ddagger}}{R}\right]. \quad \text{(A5)}$$

The temperature dependence of $k(T)$, or Q_{10} of proton permeation, is expressed as:

$$Q_{10}(T) = Exp[10 \times \partial_T \log k(T)] = Exp\left[10 \times \left(\frac{\Delta H_{Ch'}^{\ddagger}}{RT^2} + \frac{1}{T}\right)\right]. \quad \text{(A6)}$$

The access resistance

Access resistance was formalized theoretically based on geometrical and electrostatic considerations, and a simplified expression was proposed by Hall (1975) as

$$R_{AR} = \frac{\rho}{4r}, \quad \text{(A7)}$$

where ρ is the resistivity of the solution and r is the capture radius. The resistance of a hemispherical region outside a pore entrance was integrated to give the access resistance, and most of the resistance arises within close vicinity of the pore. The time for development of the access resistance can be estimated by r^2/D (Crank, 1975). For $r < 1$ nm and D (diffusion coefficient) $< 10^{-4}$ cm^2/s, the time constant is 10^{-10} s.

The access resistance is further modified by the presence of buffer. Protonated buffer distributes within the access region and supplies protons to the pore, which replenishes the limited delivery (proton supply by buffer; Fig. 2) (Decker and Levitt, 1988). This may attenuate amplitudes of the access resistance. Here, we estimate the effectiveness of the proton supply from the buffer to the pore quantitatively. The time constant for buffering is

$$\frac{1}{k_1[H^+] + k_{-1}},$$

and it is calculated as 10^{-4} to 10^{-5} s for a k_1 of 10^9–10^{10} M^{-1}/s and k_{-1} of $k_1 \times 10^{-pK}$. This value is much larger than the time constant for development of the access resistance ($\sim 10^{-10}$ s). This means that the release rate of protons from the protonated buffer is much slower than the development of access resistance. In this case, the proton supply from the protonated buffer cannot keep up with the demand. The access resistance for the voltage-gated proton channel has not been estimated quantitatively, so these theoretical predictions remain to be evaluated experimentally.

The total resistance (R_{total}) across the membrane is composed of the channel resistance (R_{Ch}) and the access resistance on both sides of the membrane (external and internal R_{AR}).

$$R_{total} = R_{Ch} + R_{AR}^{i} + R_{AR}^{o}. \quad \text{(A8)}$$

The relative contributions of R_{AR} to R_{total} were estimated by the following methods. Changes in the external R_{AR} lead to changes in R_{total}, even if R_{Ch} and internal R_{AR} are constant. The external R_{AR} can be changed by altering ρ (Eq. A7) (Hall, 1975), which is attained by perfusing extracellular solutions with higher resistivity, such as by adding concentrated nonelectrolytes (Ando et al., 2005). From the changes in the current amplitude upon exposure (the resistivity pulse method), the relative contribution of R_{AR} to R_{Ch} can be estimated by this equation:

$$\frac{I^{jump}}{I^{pre-jump}} = \frac{R_{Ch} + R_{AR}^{o} + R_{AR}^{i}}{R_{Ch} + R_{AR}^{o\prime} + R_{AR}^{i}}, \quad \text{(A9)}$$

in which $R_{AR}^{o\prime}$ represents the resistance after perfusion with a different conductivity solution. Incorporating Hall's relation for the ratio of the access resistances at different solutions, the conductance ratio can be obtained:

$$\frac{I^{jump}}{I^{pre-jump}} = \frac{1 + \dfrac{R_{Ch} + R_{AR}^{i}}{R_{AR}^{o}}}{\dfrac{R_{Ch} + R_{AR}^{i}}{R_{AR}^{o}} + \dfrac{\rho'}{\rho}}. \quad \text{(A10)}$$

We assume that the external and internal R_{AR} are identical in symmetric solutions. Based on Hall's equation, R_{AR} is determined by the conductivity and the capture radius. Therefore, the symmetric assumption is acceptable as far as the structural information of the channel is not available. Eq. A10 becomes

$$\frac{I^{jump}}{I^{pre-jump}} = \frac{2 + R_{Ch}/R_{AR}}{1 + R_{Ch}/R_{AR} + \rho'/\rho}. \quad \text{(A11)}$$

Published August 31, 2009

In this equation, the resistivities of the buffer solution were measured by a conductivity meter at different temperatures. The resistance ratio is an only unknown parameter that can be obtained through fitting the experimental data.

The Q_{10} value for resistances in series

The total conductance of the channel and access resistances in series are expressed as

$$G_{total} = \frac{G_{Ch} \times G_{AR}}{G_{AR} + 2G_{Ch}}, \tag{A12}$$

where G_{Ch} is the channel conductance and G_{AR} is the access conductance. The Q_{10} value for this conductance is

$$Q_{10}(T) = Exp\left[10 \times \partial_T \log(G_{total})\right] = Exp\left[10 \times \frac{2G_{Ch}G_{AR}' + G_{AR}^{2}G_{Ch}'}{G_{AR}^{2}G_{Ch} + 2G_{AR}G_{Ch}^{2}}\right]. \tag{A13}$$

G_{Ch} was replaced by $k(T)$ and G_{AR} was replaced by Eq. 12, in which ρ is expressed by $1/(A\,Exp[-B/T])$. Then, $Q_{10}(T)$ is expressed as

$$Q_{10} = Exp\left[\frac{10}{T^2}\left(B + \frac{A\left(\frac{\Delta H_{Ch}^{\ddagger}}{R} + T - B\right)Exp\left[\frac{\Delta H_{Ch}^{\ddagger}}{RT}\right]}{AExp\left[\frac{\Delta H_{Ch}^{\ddagger}}{RT}\right] + 2\omega_C \frac{k_B T}{h} Exp\left[\frac{\Delta S_{Ch}^{\ddagger}}{R} + \frac{B}{T}\right]}\right)\right], \tag{A14}$$

where $\Delta H_{Ch}^{\ddagger}$ is the activation enthalpy, $\Delta S_{CH}^{\ddagger}$ is the activation entropy, and ω_C is the frequency factor for the channel. A and B can be obtained from the resistivity measurements at different temperatures. The fitting of the three unknown parameters ($\Delta H^{\ddagger}_{Ch}$, $\Delta S^{\ddagger}_{Ch}$, and ω_C) to the measured Q_{10} values was performed.

We would like to thank O.S. Andersen, M. Iwamoto, T. Konno, H. Shimizu, S. Irie, and C. Edwards for discussion. We also thank J. Kawawaki and H. Nakagawa for technical assistance and T. Goto for secretarial assistance.

This work is supported by a Grant-in-Aid for Scientific Research from the Ministry of Education, Culture, Sports, Science and Technology (Japan).

Lawrence G. Palmer served as editor.

Submitted: Submitted: 3 February 2009
Accepted: Accepted: 23 July 2009

REFERENCES

Agmon, N. 1995. The Grotthuss mechanism. *Chem. Phys. Lett.* 244:456–462.

Agmon, N. 1996. Hydrogen bonds, water rotation and proton mobility. *J. Chim. Phys.* 93:1714–1736.

Agmon, N. 1999. Proton solvation and proton mobility. *Isr. J. Chem.* 39:493–502.

Aguilella-Arzo, M., V.M. Aguilella, and R.S. Eisenberg. 2005. Computing numerically the access resistance of a pore. *Eur. Biophys. J.* 34:314–322.

Akeson, M., and D.W. Deamer. 1991. Proton conductance by the gramicidin water wire. Model for proton conductance in the F1F0 ATPases? *Biophys. J.* 60:101–109.

Andersen, O.S. 1983. Ion movement through gramicidin A channels. Studies on the diffusion-controlled association step. *Biophys. J.* 41:147–165.

Andersen, O.S. 1984. Gramicidin channels. *Annu. Rev. Physiol.* 46:531–548.

Ando, H., M. Kuno, H. Shimizu, I. Muramatsu, and S. Oiki. 2005. Coupled K+–water flux through the HERG potassium channel measured by an osmotic pulse method. *J. Gen. Physiol.* 126:529–538.

Bamberg, E., and P. Läuger. 1974. Temperature-dependent properties of gramicidin A channels. *Biochim. Biophys. Acta.* 367:127–133.

Berg, H.C., and E.M. Purcell. 1977. Physics of chemoreception. *Biophys. J.* 20:193–219.

Berry, R.S., S.A. Rice, and J. Ross. 2000. Physical Chemistry. 2nd Ed. Oxford University Press, New York. 1080 pp.

Braun-Sand, S., A. Burykin, Z.T. Chu, and A. Warshel. 2005. Realistic simulations of proton transport along the gramicidin channel: demonstrating the importance of solvation effects. *J. Phys. Chem. B.* 109:583–592.

Byerly, L., and Y. Suen. 1989. Characterization of proton currents in neurones of the snail, Lymnaea stagnalis. *J. Physiol.* 413:75–89.

Cherny, V.V., R. Murphy, V. Sokolov, R.A. Levis, and T.E. DeCoursey. 2003. Properties of single voltage-gated proton channels in human eosinophils estimated by noise analysis and by direct measurement. *J. Gen. Physiol.* 121:615–628.

Chernyshev, A., and S. Cukierman. 2002. Thermodynamic view of activation energies of proton transfer in various gramicidin A channels. *Biophys. J.* 82:182–192.

Crank, J. 1975. The Mathematics of Diffusion. 2nd Ed. Clarendon Press, Oxford, UK. 424 pp.

Cukierman, S. 2000. Proton mobilities in water and in different stereoisomers of covalently linked gramicidin A channels. *Biophys. J.* 78:1825–1834.

Day, T.J.F., U.W. Schmitt, and G.A. Voth. 2000. The mechanism of hydrated proton transfer in water. *J. Am. Chem. Soc.* 122:12027–12028.

de Grotthuss, C.J.T. 1806. Sur la décomposition de l'eau et des corp qu'elle tient en dissolution à l'aide de l'électricité galvanique. *Annales de Chimie.* LVIII:54–74.

Decker, E.R., and D.G. Levitt. 1988. Use of weak acids to determine the bulk diffusion limitation of H^+ ion conductance through the gramicidin channel. *Biophys. J.* 53:25–32.

DeCoursey, T.E. 2003. Voltage-gated proton channels and other proton transfer pathways. *Physiol. Rev.* 83:475–579.

DeCoursey, T.E. 2008. Voltage-gated proton channels: what's next? *J. Physiol.* 586:5305–5324.

DeCoursey, T.E., and V.V. Cherny. 1996. Effects of buffer concentration on voltage-gated H^+ currents: does diffusion limit the conductance? *Biophys. J.* 71:182–193.

DeCoursey, T.E., and V.V. Cherny. 1998. Temperature dependence of voltage-gated H^+ currents in human neutrophils, rat alveolar epithelial cells, and mammalian phagocytes. *J. Gen. Physiol.* 112:503–522.

Eigen, M. 1964. Proton transfer, acid-base catalysis, and enzymatic hydrolysis. Part 1: elementary processes. *Angew. Chem. Int. Ed. Engl.* 3:1–72.

Eigen, M., W. Kruse, G. Maass, and L. De Maeyer. 1964. Rate constants of proteolytic reactions in aqueous solution. *Prog. React. Kinet.* 2:287–318.

Fersht, A. 1999. Structure and Mechanism in Protein Science. W.H. Freeman and Company, New York. 650 pp.

Published August 31, 2009

Gordienko, D.V., M. Tare, S. Parveen, C.J. Fenech, C. Robinson, and T.B. Bolton. 1996. Voltage-activated proton current in eosinophils from human blood. *J. Physiol.* 496:299–316.

Grygorczyk, R. 1987. Temperature dependence of Ca^{2+}-activated K^+ currents in the membrane of human erythrocytes. *Biochim. Biophys. Acta.* 902:159–168.

Gutfreund, H. 1995. Kinetics for the Life Sciences: Receptors, Transmitters and Catalysts. Cambridge University Press, Cambridge, UK. 346 pp.

Hall, J.E. 1975. Access resistance of a small circular pore. *J. Gen. Physiol.* 66:531–532.

Hänggi, P., P. Talkner, and M. Borkovec. 1990. Reaction-rate theory: fifty years after Kramers. *Rev. Mod. Phys.* 62:251–341.

Heinemann, S.H., and F.J. Sigworth. 1989. Estimation of Na^+ dwell time in the gramicidin A channel. Na^+ ions as blockers of H^+ currents. *Biochim. Biophys. Acta.* 987:8–14.

Henderson, L.M., J.B. Chappell, and O.T. Jones. 1987. The superoxide-generating NADPH oxidase of human neutrophils is electrogenic and associated with an H^+ channel. *Biochem. J.* 246:325–329.

Hille, B. 1968. Pharmacological modifications of the sodium channels of frog nerve. *J. Gen. Physiol.* 51:199–219.

Hille, B. 2001. Ion Channels of Excitable Membranes. 3rd Edition. Sinauer Associates Inc., Sunderland, MA. 814 pp.

Hladky, S.B. 1984. Ion currents through pores. The roles of diffusion and external access steps in determining the currents through narrow pores. *Biophys. J.* 46:293–297.

Hoffmann, H.M., and V.E. Dionne. 1983. Temperature dependence of ion permeation at the endplate channel. *J. Gen. Physiol.* 81:687–703.

Keener, J., and J. Sneyd. 1998. Mathematical Physiology. Springer-Verlag, New York. 792 pp.

Koeppe, R.E.I.I., II, and O.S. Anderson. 1996. Engineering the gramicidin channel. *Annu. Rev. Biophys. Biomol. Struct.* 25:231–258.

Kramers, H.A. 1940. Brownian motion in a field of force and the diffusion model of chemical reactions. *Physica.* 7:284–304.

Kuno, M., J. Kawawaki, and F. Nakamura. 1997. A highly temperature-sensitive proton current in mouse bone marrow–derived mast cells. *J. Gen. Physiol.* 109:731–740.

Läuger, P. 1976. Diffusion-limited ion flow through pores. *Biochim. Biophys. Acta.* 455:493–509.

Limbach, H.H., J. Miguel Lopez, and A. Kohen. 2006. Arrhenius curves of hydrogen transfers: tunnel effects, isotope effects and effects of pre-equilibria. *Philos. Trans. R. Soc. Lond. B Biol. Sci.* 361:1399–1415.

Mahaut-Smith, M.P. 1989. The effect of zinc on calcium and hydrogen ion currents in intact snail neurones. *J. Exp. Biol.* 145:455–464.

Milburn, T., D.A. Saint, and S.H. Chung. 1995. The temperature dependence of conductance of the sodium channel: implications for mechanisms of ion permeation. *Receptors Channels.* 3:201–211.

Miller, C., N. Stahl, and M. Barrol. 1988. A thermodynamic analysis of monovalent cation permeation through a K(+)-selective ion channel. *Neuron.* 1:159–164.

Morgan, D., V.V. Cherny, R. Murphy, W. Xu, L.L. Thomas, and T.E. DeCoursey. 2003. Temperature dependence of NADPH oxidase in human eosinophils. *J. Physiol.* 550:447–458.

Morihata, H., J. Kawawaki, H. Sakai, M. Sawada, T. Tsutada, and M. Kuno. 2000a. Temporal fluctuations of voltage-gated proton currents in rat spinal microglia via pH-dependent and -independent mechanisms. *Neurosci. Res.* 38:265–271.

Morihata, H., F. Nakamura, T. Tsutada, and M. Kuno. 2000b. Potentiation of a voltage-gated proton current in acidosis-induced swelling of rat microglia. *J. Neurosci.* 20:7220–7227.

Oiki, S., R.E. Koeppe II, and O.S. Andersen. 1995. Voltage-dependent gating of an asymmetric gramicidin channel. *Proc. Natl. Acad. Sci. USA.* 92:2121–2125.

Peskoff, A., and D.M. Bers. 1988. Electrodiffusion of ions approaching the mouth of a conducting membrane channel. *Biophys. J.* 53:863–875.

Ramsey, I.S., M.M. Moran, J.A. Chong, and D.E. Clapham. 2006. A voltage-gated proton-selective channel lacking the pore domain. *Nature.* 440:1213–1216.

Robinson, R.A., and R.H. Stokes. 2002. Electrolyte Solutions. 2nd Revised Ed. Dover Publications, Mineola, NY. 590 pp.

Sasaki, M., M. Takagi, and Y. Okamura. 2006. A voltage sensor-domain protein is a voltage-gated proton channel. *Science.* 312:589–592.

Sawada, M., F. Imai, H. Suzuki, M. Hayakawa, T. Kanno, and T. Nagatsu. 1998. Brain-specific gene expression by immortalized microglial cell-mediated gene transfer in the mammalian brain. *FEBS Lett.* 433:37–40.

Schumaker, M.F. 2003. Numerical framework models of single proton conduction through gramicidin. *Front. Biosci.* 8:s982–s991.

Schumaker, M.F., R. Pomès, and B. Roux. 2000. A combined molecular dynamics and diffusion model of single proton conduction through gramicidin. *Biophys. J.* 79:2840–2857.

Sitsapesan, R., R.A. Montgomery, K.T. MacLeod, and A.J. Williams. 1991. Sheep cardiac sarcoplasmic reticulum calcium-release channels: modification of conductance and gating by temperature. *J. Physiol.* 434:469–488.

Starace, D.M., and F. Bezanilla. 2004. A proton pore in a potassium channel voltage sensor reveals a focused electric field. *Nature.* 427:548–553.

Stojilkovic, K.S., A.M. Berezhkovskii, V.Y. Zitserman, and S.M. Bezrukov. 2003. Conductivity and microviscosity of electrolyte solutions containing polyethylene glycols. *J. Chem. Phys.* 119:6973–6978.

Swanson, J.M.J., C.M. Maupin, H. Chen, M.K. Petersen, J. Xu, Y. Wu, and G.A. Voth. 2007. Proton solvation and transport in aqueous and biomolecular systems: insights from computer simulations. *J. Phys. Chem. B.* 111:4300–4314.

Swietach, P., M. Zaniboni, A.K. Stewart, A. Rossini, K.W. Spitzer, and R.D. Vaughan-Jones. 2003. Modelling intracellular H^+ ion diffusion. *Prog. Biophys. Mol. Biol.* 83:69–100.

Thomas, R.C., and R.W. Meech. 1982. Hydrogen ion currents and intracellular pH in depolarized voltage-clamped snail neurones. *Nature.* 299:826–828.

Urry, D.W., S. Alonso-Romanowski, C.M. Venkatachalam, R.J. Bradley, and R.D. Harris. 1984. Temperature dependence of single channel currents and the peptide libration mechanism for ion transport through the gramicidin A transmembrane channel. *J. Membr. Biol.* 81:205–217.

Zifarelli, G., P. Soliani, and M. Pusch. 2008. Buffered diffusion around a spherical proton pumping cell: a theoretical analysis. *Biophys. J.* 94:53–62.

J Mol Neurosci
DOI 10.1007/s12031-009-9187-6

Interleukin-6 Induces Prostaglandin E_2 Synthesis in Mouse Astrocytes

Toshiyuki Chikuma · Tetsuya Yoshimoto · Masahiro Ohba · Makoto Sawada · Takeshi Kato · Tomoaki Sakamoto · Yukio Hiyama · Hiroshi Hojo

Received: 9 November 2008 / Accepted: 16 February 2009

Abstract The physiological function of interleukin-6 within the central nervous system (CNS) is complex; interleukin-6 exerts neurotrophic and neuroprotective effects and yet can also function as a mediator of inflammation, demyelination, and astrogliosis depending on the cellular context. However, the roles of interleukin-6 in astrocytes are poorly understood. In the present study, we investigated the effect of the pro-inflammatory cytokine interleukin-6 on the production of the inflammatory mediator prostaglandin E_2 in mouse astrocytes. Interleukin-6 stimulated prostaglandin E_2 production in a time-dependent fashion via a rapid and transient induction of cyclooxygenase-2 messneger RNA, followed by cyclooxygenase-2 protein synthesis. Interleukin-6 may act on the nervous system by interacting with its specific soluble interleukin-6 receptor and the signal transducer 130-kDa glycoprotein. Simultaneous treatment of astrocytes with interleukin-6 and soluble interleukin-6 receptor caused marked induction of prostaglandin E_2 synthesis, and this effect was suppressed by adding a neutralizing antibody against soluble interleukin-6 receptor. Furthermore, the mouse 130-kDa glycoprotein antibody suppressed prostaglandin E_2 formation induced by interleukin-6, as well as interleukin-6/soluble interleukin-6 receptor complexes, in a dose-dependent manner. These results indicate that interleukin-6/soluble interleukin-6 receptor complexes and the signal transducer 130-kDa glycoprotein play an important role in the regulation of cyclooxygenase-2 expression and subsequent prostaglandin E_2 formation in mouse astrocytes and that interleukin-6 is an important regulator of immune and inflammatory processes in the CNS.

Keywords Interleukin-6 · Prostaglandin E_2 · Cyclooxygenase-2 · Soluble interleukin-6 receptor · 130-kDa glycoprotein · Astrocytes

Abbreviations

AD	Alzheimer's disease
ALS	Amyotrophic lateral sclerosis
bFGF	Basic fibroblast growth factor
COX	Cyclooxygenase
$cPLA_2$	Cytosolic phospholipase A_2
MEM	Minimum essential medium
EIA	Enzyme immunoassay
FBS	Fetal bovine serum
gp130	130-kDa glycoprotein
IL-1 β	Interleukin-1β
IL-6	Interleukin-6
IL-6R	Interleukin-6 receptor

T. Chikuma · T. Yoshimoto · M. Ohba · H. Hojo
Department of Hygienic Chemistry,
Showa Pharmaceutical University,
Machida-shi,
Tokyo 194-8543, Japan

M. Sawada
Department of Brain Life Science, Research Institute of Environmental Medicine, Nagoya University,
Nagoya 464-8601, Japan

T. Kato
Laboratory of Molecular Recognition, Graduate School of Integrated Science, Yokohama City University,
Yokohama 236-0027, Japan

T. Sakamoto · Y. Hiyama
Division of Drugs, National Institute of Health Sciences,
Tokyo 158-8501, Japan

T. Chikuma (✉)
Department of Pharmaceutical Analytical Chemistry,
Showa Pharmaceutical University,
3-3165 Higashi-tamagawagakuen, Machida-shi,
Tokyo 194-8543, Japan
e-mail: chikuma@ac.shoyaku.ac.jp

Published online: 10 March 2009

JAK	Janus kinase
LPS	Lipopolysaccharide
PBS	Ca^{2+}- and Mg^{2+}-free phosphate-buffered saline
PDGF	Platelet-derived growth factor
PGE_2	Prostaglandin E_2
PGs	Prostaglandins
sIL-6R	Soluble interleukin-6 receptor
STAT	Signal transducers and activators of transcription
TGF-β	Transforming growth factor-β
TNF-α	Tumor necrosis factor-α
TPBS	PBS containing 0.05% Tween 20

Introduction

Prostaglandins (PGs) are major lipid mediators produced by cyclooxygenase (COX) activity. They play important modulatory roles in various cells throughout the body. Prostaglandin E_2 (PGE_2) is the most abundant prostaglandin in the brain (Bishai and Coceani 1992) and is considered to play an essential role in several pathological states. In the central nervous system (CNS), PGE_2 is responsible for fever induction (Ushikubi et al. 1998) and participates in eliciting pain hypersensitivity (Samad et al. 2001). In addition, elevated PGE_2 levels have been detected in the cerebrospinal fluid of patients with Alzheimer's disease (AD; Montine et al. 1999), stroke (Jacobs et al. 1987), ischemia (Nogawa et al. 1997), and amyotrophic lateral sclerosis (ALS; Almer et al. 2001). When cells and tissue are exposed to various pro-inflammatory stimuli, arachidonic acid is liberated from membrane phospholipids and converted to PGs by the action of COX enzymes.

COX is the key enzyme in the metabolic pathway leading to PG and thromboxane A_2 formation from arachidonic acid (Dubois et al. 1998). Two isoforms have been identified, COX-1 and COX-2 (Smith et al. 1996). COX-1 is constitutively expressed in nearly all normal mammalian tissues and mediates the synthesis of PGs required for physiological tissue homeostasis. By contrast, COX-2 is constitutively expressed in the brain in specific neuronal populations where it seems to be regulated by synaptic activity (Hayaishi 1991; Yamagata et al. 1993; Marcheselli and Bazan 1996). However, in inflammatory pathological conditions, the immune-competent cells of the CNS, astrocytes and microglia, are likely to be the major sources of PGs following induction of COX-2 (Minghetti and Levi 1995; O'Banion et al. 1996; Bauer et al. 1997; Vane et al. 1998; Minghetti et al. 1999; Molina-Holgado et al. 2000).

Interleukin-6(IL-6) was initially described as a central mediator of the immune system, hemopoiesis, and acute phase reaction. IL-6 is a member of the neurocytokine family, which also includes ciliary neurotrophic factor, leukemia inhibitory factor, oncostatin M, and cardiotrophin-1. These molecules have overlapping biological activities: they possess similar secondary structures and exert their activities through related multisubunit receptors (Rose-John and Heinrich 1994; Heinrich et al. 1998). The IL-6 receptor (IL-6R), gp80, can exist either as a membrane-bound protein or a soluble protein (sIL-6R; Kishimoto et al. 1994). Binding of IL-6 to either the membrane-bound or soluble form of IL-6R promotes homodimerization of a 130-kDa glycoprotein (gp130) molecule. Both neurons and glia can produce IL-6 (Gadient and Otten 1994; Sawada et al. 1995; Marz et al. 1998; Their et al. 1999).

Astrocytes are the major cell type in the CNS. These cells not only supply nutrients to neurons but also mediate inflammatory responses in the CNS. Following CNS injury or an immune/inflammatory challenge, astrocytes undergo a phenotypic alteration—a response known as activation. The activated astrocytes then release cytokines and other pro-inflammatory mediators, including PGs. These released substances communicate with such neighboring cells as neurons and microvascular cells. Astrocytes are a major source of PGs in the CNS: in culture, these cells synthesize up to 20 times more PGs than do neurons (Seregi et al. 1984). Their ability to produce PGE_2 upon stimulation with interleukin-1β (IL-1β), ATP, platelet-activating factor, transforming growth factor-β (TGF-β), oncostatin M, tumor necrosis factor-α (TNF-α), or lipopolysaccharide (LPS) has been documented (Fontana et al. 1982; O'Banion et al. 1996; Ishimoto et al. 1997; Luo et al. 1998; Mollace et al. 1998; Pistritto et al. 1998, 1999; Molina-Holgado et al. 2000; Teather et al. 2002; Repovic et al. 2003; Xu et al. 2003). However, PGE_2 formation upon stimulation of astrocytes with IL-6 has not been investigated. In the present study, we used purified mouse astrocytes to investigate the effects of IL-6 on PGE_2 synthesis and the expression of COX-2, which catalyzes PG formation. In addition, possible roles of sIL-6R and gp130 in PGE_2 formation were also explored.

Materials and Methods

Materials

PGE_2, recombinant mouse IL-6, D-glucose, and bovine pancreas insulin were purchased from Sigma Chemical Co. (St. Louis, MO, USA). DNase I and RNase inhibitor were obtained from Takara-bio Co. (Tokyo, Japan). Oligo(dt) primer and ribonuclease H were purchased from Invitrogen (Carlsbad, CA, USA). Biotin-conjugated goat anti-rabbit IgG and streptavidin–horseradish peroxidase (HRP) were obtained from Dako Cytomation (Kyoto, Japan). Anti-human sIL-6R goat antibody and anti-mouse gp130 goat antibody were purchased from R&D Systems (Minneapolis,

MN, USA). Recombinant human sIL-6R and anti-mouse COX-2 rabbit antibody were purchased from PreproTec EC Ltd. (London, UK) and Cayman Chemical Co. (Ann Arbor, MI, USA), respectively. All other reagents were purchased from commercial sources and generally were the highest purity available.

Cell Culture

Astrocytes were prepared from mixed primary glial cell cultures obtained from newborn C57BL/B6 mouse brain as previously described (Sawada et al. 1993). The purity of the astrocytes thus obtained was greater than 95%, as estimated by indirect immunofluorescence using anti-glial fibrillary acidic protein antibody. These astrocyte-enriched cultures did not contain neurofilament-positive neurons and the contamination of microglia was negligible. The cells were cultured in Eagle's minimum essential medium (Eagle's MEM; Sigma) containing 10% heat-inactivated fetal bovine serum (FBS; JRH Biosciences, Lenexa, KS, USA), 2 mg/ml glucose, 5 μg/ml bovine insulin, 100 IU/ml penicillin, and 100 μg/ml streptomycin (Gibco BRL, Rockville, MD, USA) at 37°C in an atmosphere of 5% CO_2 and 95% air and then subcultured every 3 days before the experiments were performed. For total RNA extraction, cells were plated in 10-cm diameter dishes (Falcon: 5×10^5 cells/dish in 10 ml of culture medium); for the PGE_2 enzyme immunoassay (EIA), cells were plated in 24-well plates (Iwaki: 4×10^4 cells/well in 400 μl of culture medium) and then cultured for 2 days until they were nearly confluent. The medium was then replaced with fresh medium, and cells were activated with or without various concentrations of IL-6 or other reagents followed by further culturing for the indicated periods.

Measurement of PGE_2

PGE_2 was assayed using a specific EIA system (Amersham, UK). Briefly, supernatants of cultured astrocytes or standard PGE_2 were incubated for 1 h with specific anti-PGE_2 reagent and peroxidase-labeled PGE_2 in pre-packed 96-well plates containing a goat anti-mouse solid phase. Unlabeled PGE_2 (standard or unknown) and PGE_2–peroxidase complex competed for a limited number of binding sites on PGE_2-specific antibodies, and the amount of peroxidase-labeled ligand was inversely proportional to the concentration of added standard or unknown. After washing four times with washing buffer, tetramethylbenzidine/hydrogen peroxide single pot substrate was added and incubated for 30 min. Addition of acid solution stopped the reaction, and the resultant color was read at 450 nm in a microtiter plate photometer. The concentration of unlabeled PGE_2 in a sample was determined by interpolation from a standard curve, and the data are expressed as pg PGE_2 in each well.

Western Blot Analysis

Cells were exposed to 10 ng/ml IL-6 for the indicated periods of time. Cells were washed three times with ice-cold Ca^{2+}- and Mg^{2+}-free phosphate-buffered saline (PBS) and lysed in 100 mM phosphate buffer (pH 7.4) containing 1 mM EDTA and 0.05% Triton X-100 (*v*/*v*). The cell lysates were centrifuged at 10,000×*g* for 10 min at 4°C and the resultant supernatants were used for analysis. Protein concentration was determined by the Bradford method (Bradford 1976) using bovine serum albumin as a standard protein. For Western blotting, 10 μg of cell protein from each sample for COX-2 detection was subjected to sodium dodecyl sulfate–polyacrylamide gel electrophoresis on an 8% separating gel under reducing conditions. Proteins were then transferred onto poly(vinylidene difluoride) membranes (Millipore, Bedford, MA, USA) by semi-dry blotting. The electroblotted membranes were blocked for 1 h in 2% Block Ace solution (Dainippon Pharmaceutical, Osaka, Japan) and then incubated with anti-mouse COX-2 rabbit antibody (1:32,000) for 1.5 h at room temperature. Subsequently, the membranes were washed three times in PBS containing 0.05% Tween 20 (TPBS) and incubated for 45 min with biotin-conjugated goat anti-rabbit IgG (1:50,000). After washing membranes three times with TPBS, they were incubated with streptavidin-HRP (1:50,000) for 45 min at room temperature and the resulting protein bands were visualized using ECL Plus Western blotting detection reagents (GE Healthcare Bio-Sciences, Piscataway, NJ, USA) according to the manufacturer's instructions. Immunoblots were digitized using Image-Master ID Elite (GE Healthcare Bio-Sciences) and expressed as fold induction compared with control cultures.

RNA Extraction and Reverse Transcription PCR Analysis

Total RNA was extracted from astrocytes using ISOGEN (Nippongene Co., Tokyo, Japan) according to the manufacturer's instructions. The purity of the RNA preparations was checked by measuring the absorbance ratio at 260/280 nm. Each RNA sample was subjected to first-strand complementary DNA (cDNA) synthesis using SuperScript II reverse transcriptase (Invitrogen) following the protocol suggested by the manufacturer. Reactions were performed at 42°C for 50 min. cDNA samples (0.5 μl) were amplified for 30 (β-actin) or 35 cycles (COX-2) in an Astec PC-800 thermal cycler using Taq DNA polymerase and polymerase chain reaction (PCR) reagents (Takara-bio Co.), with primers specific for β-actin and COX-2, in a total volume of 25 μl. The PCR amplimer pairs for the analysis of COX-2 cDNA were 5′-CATGGGTGTGAAGGGAAATAAG-3′ (sense) and 5′-TGAGATAGTGACCGTGGGGG-3′ (antisense), which were complementary to the conserved